

A MINOT-based Study of Gamma-ray emission from SPT-CL J2012-5649/Abell 3667

Siddhant Manna^{1,*} and Shantanu Desai^{1,†}

¹ *Department of Physics, IIT Hyderabad Kandi, Telangana 502284, India*

We present an analysis of the non-thermal properties of the merging galaxy cluster SPT-CL J2012-5649/Abell 3667 ($z = 0.0556$, $M_{500} = 7.16 \times 10^{14} M_{\odot}$) using the MINOT non-thermal emission modelling framework. The predicted hadronic gamma-ray flux from pp interactions in the 1–300 GeV band is $2.82 \times 10^{-11} \text{ cm}^{-2} \text{ s}^{-1}$ within R_{500} , rising to $1.15 \times 10^{-10} \text{ cm}^{-2} \text{ s}^{-1}$ at the truncation radius ($3.7 R_{500}$), in order-of-magnitude agreement with the Fermi-LAT reported flux of $1.3 \times 10^{-10} \text{ cm}^{-2} \text{ s}^{-1}$. Approximately 76% of the predicted hadronic flux originates from beyond R_{500} . The IC contribution from cosmic-ray electrons is subdominant relative to the hadronic π^0 -decay gamma-ray component by a factor of ~ 20 in the 1–300 GeV energy band, and therefore does not contribute significantly to the observable signal. Although the expected hadronic flux is in approximate agreement with the observed Fermi-LAT flux level in the 1–300 GeV band, the observed spectral index ($\Gamma = -3.61 \pm 0.33$) is in tension with the hadronic prediction ($\Gamma \approx -2.4$ to -2.6).

I. INTRODUCTION

Galaxy clusters are formed through the gravitational collapse of overdense regions that existed in the early universe. Over cosmic time, density perturbations cause these regions to gravitationally attract surrounding matter, gradually building up into clumps and filaments that eventually coalesce into clusters [1]. As a result, galaxy clusters represent the largest structures in the universe that are both gravitationally bound and virialized, making them exceptional laboratories for investigating cosmology [2–5] and fundamental physics [6–10]. Observationally, galaxy clusters have been detected across a broad range of wavelengths, spanning from radio [11] to hard X-rays [12]. Over the last two decades, dedicated surveys conducted in the optical, X-ray, and microwave bands have significantly expanded the known cluster population, enabling a wide variety of cosmological and astrophysical investigations, often through multi-wavelength analyses.

Although initial searches for gamma-ray emission from galaxy clusters using Fermi-LAT telescope reported null results [13–15], in recent years several groups have found a gamma-ray signal from clusters. In [16], we performed a systematic search for gamma-ray emission from 300 galaxy clusters selected from the SPT-SZ survey using approximately 15 years of Fermi-LAT data in the 1–300 GeV energy range. Our analysis reported a $\sim 6.1\sigma$ gamma-ray detection from the cluster SPT-CL J2012–5649, coincident with Abell 3667 with emission primarily observed between 1–10 GeV. However, because several radio galaxies lie within the Fermi-LAT point spread function around the cluster, the study could not conclusively establish the cluster origin of the observed gamma-ray signal. Subsequently, Harale and Paul [17] reported a $\sim 4\sigma$ excess of diffuse gamma-ray emission from the dynamically active galaxy cluster Abell 119 using 14 years of Fermi-LAT data. The detected excess was spatially offset from the cluster center and was found to be better described by an extended emission model, suggesting a possible origin from nonthermal hadronic processes in the intracluster medium. Recently, Li and Han [18] carried out a systematic analysis of 65 galaxy clusters using 16 years of Fermi-LAT observations in the 0.5–500 GeV range and reported significant gamma-ray excesses from the clusters Abell 2065 and Abell 2244 with local significances of $\sim 5\sigma$. Their study concluded that the detected emission is unlikely to originate from dark matter annihilation and is more plausibly associated with hadronic cosmic-ray interactions within the intracluster medium. They also reported a possible gamma-ray excess from the merging galaxy cluster Abell 3667 with $TS \sim 24.3$ detected near the cluster center, with an integral photon flux of $(2.93 \pm 0.69) \times 10^{-10} \text{ ph cm}^{-2} \text{ s}^{-1}$ in the 0.5–500 GeV energy range. However, the detected emission may be associated with nearby radio sources, and therefore the cluster origin of the gamma-ray signal remains uncertain.

In a series of studies based on stacked Fermi-LAT observations of galaxy clusters, U. Keshet [19–21] reported statistically significant gamma-ray excesses associated with both cluster virial shocks and central regions. The 2018 study [19] detected a gamma-ray ring at the virial shock radius of stacked clusters with a significance of $\sim 5.8\sigma$, interpreted as IC emission from relativistic electrons accelerated at virial shocks. More recent analyses [20, 21] reported extended central gamma-ray excesses consistent with hadronic cosmic-ray interactions in the

*Email:ph22resch11006@iith.ac.in

†Email:shntn05@gmail.com

intracluster medium, along with excess gamma-ray sources near cluster virial radii potentially associated with radio relics and merger-driven substructures. Subsequently, we also carried out a stacked analysis of SPT-SZ galaxy clusters using 16.4 years of Fermi-LAT observations and reported a statistically significant cumulative gamma-ray signal with $TS = 75.2$, corresponding to a significance of $\sim 8.4\sigma$ [22]. The derived stacked spectrum is well described by a power-law with spectral index -2.59 ± 0.20 . Our study suggested that the strong cumulative signal is likely dominated by AGN-containing clusters, whereas the lower- TS cluster subsample shows characteristics broadly consistent with diffuse hadronic emission from the intracluster medium.

Several physical mechanisms capable of producing gamma-ray emission within galaxy clusters have been proposed in the literature, which we briefly summarize below. Galaxy clusters harbor dense concentrations of galaxies, non-baryonic dark matter (comprising roughly 80% of the total mass), and hot diffuse gas (accounting for approximately 10–15%). They also serve as vast reservoirs of high-energy relativistic cosmic rays (CRs) both electrons and protons permeating the hot, ionized intracluster medium (ICM) [23, 24]. Observational evidence for the acceleration of cosmic ray electrons is provided by radio relics detected within merging clusters [24, 25], which are believed to arise from merger-driven shock waves capable of boosting particles to extreme energies. Such energetic particles can give rise to gamma-ray emission through several channels, including Inverse Compton (IC) scattering of relativistic electrons off CMB photons, non-thermal bremsstrahlung radiation, and the decay of neutral pions produced when cosmic ray protons interact with ICM gas [26–30]. In a recent study, the cumulative gamma-ray flux from galaxy clusters was estimated by coupling cosmological MHD simulations with cosmic ray transport modeling up to redshift $z \leq 5$, revealing that this integrated flux could account for as much as 100% of the diffuse gamma-ray background at those redshifts [31]. Given that the dominant mass component in galaxy clusters is cold dark matter, gamma-ray signals could also arise from the annihilation of dark matter WIMPs within cluster halos [13, 32, 33]. In addition to ICM-related emission processes, gamma rays may also originate from star-forming activity occurring in galaxies that are members of the cluster [34].

Both classes of emission require populations of ultra-relativistic cosmic ray electrons (CRe) emitting synchrotron radiation in the μG -level magnetic fields of the ICM. The spectral and morphological properties of the radio emission, combined with X-ray observations of the thermal gas, provide constraints on the magnetic field strength and the CRe energy distribution but cannot alone distinguish between leptonic (direct CRe acceleration) and hadronic (CRe produced as secondary products of cosmic ray protons (CRp)–ICM proton interactions) origins for the emitting particles [30, 35, 36].

Gamma-ray observations offer a powerful complementary probe of the non-thermal ICM. Hadronic interactions between CRp and thermal protons produce neutral pions that decay into gamma-ray photon pairs ($p + p \rightarrow \pi^0 \rightarrow \gamma + \gamma$), generating a high-energy signal that scales as the product of the CRp and gas densities integrated over the cluster volume [35, 37, 38]. The predicted hadronic gamma-ray flux therefore provides a direct handle on the CRp energy content and spatial distribution in the ICM. In addition, IC scattering of CRe off the cosmic microwave background (CMB) produces gamma-ray emission at energies accessible to the Fermi Large Area Telescope (Fermi-LAT) providing an independent constraint on the leptonic CR population [30, 39, 40].

The non-detections from gamma-ray searches using Fermi-LAT in the first decade after launch [13–15] place upper limits on the CRp-to-thermal energy ratio of order $X_{\text{CRp}} \lesssim 10^{-2}$, broadly consistent with predictions from cosmological simulations of structure formation [28, 38]. These upper limits motivate detailed, cluster-by-cluster modeling of the expected non-thermal emission, particularly for systems with well-characterized X-ray thermodynamic structure and prominent non-thermal radio features.

Abell 3667 (hereafter A3667) is one of the most compelling targets for such a study, given that gamma-ray emission with $\geq 5\sigma$ significance was recently detected [16]. It is a massive ($M_{500} = 7.16 \times 10^{14} M_{\odot}$), dynamically disturbed galaxy cluster at redshift $z = 0.0556$, undergoing a major binary merger [41]. A3667 hosts prominent merger-driven shocks and double radio relic systems [42–45], with two large-scale arc-shaped relics. The cluster also exhibits prominent X-ray cold fronts [46], providing direct evidence for complex merger history. The combination of a well-studied radio relic system, deep archival X-ray data, and the ongoing merger morphology makes A3667 an ideal laboratory for multiwavelength non-thermal emission modeling.

Multi-band observational constraints on A3667 now span from hard X-rays to GeV gamma-rays. Fermi-LAT observations have reported a gamma-ray signal in the 1–300 GeV band with photon flux $\sim 1.3 \times 10^{-10} \text{ cm}^{-2} \text{ s}^{-1}$ and a steep spectral index $\Gamma = -3.61 \pm 0.33$ [16, 47]. However, the LAT emission is confined within $\sim 0.2 R_{200}$ and detected only in the 1–10 GeV band [16]. Yet, MeerKAT data reveal several compact radio sources within a few arcminutes of the cluster center [45]. To clarify the nature of the emission, multi-wavelength and multi-instrument follow-up studies have been pursued. Archival COMPTEL data show no evidence of MeV emission [48], while INTEGRAL constrains the hard X-ray and soft gamma-ray emission in the 3–300 keV band [49]. A dedicated analysis with the DArk Matter Particle Explorer (DAMPE) [50–52] using point-source, radial-disk, and radial-Gaussian models over 3 GeV–1 TeV likewise revealed no significant signal within R_{200} , yielding 95% C.L. upper limits of $\sim 10^{-6}$ – $10^{-4} \text{ MeV cm}^{-2} \text{ s}^{-1}$ consistent with LAT measurements [53].

For A3667, previous hard X-ray studies have reported fluxes in the range of $\sim 10^{-12}$ – $10^{-11} \text{ erg cm}^{-2} \text{ s}^{-1}$. Using combined *XMM-Newton* and *Swift*/BAT observations, Ajello et al. [54] showed that the 50–100 keV

emission can be modeled either by a hot thermal component or by a power law with photon index $\Gamma \approx 1.8$, corresponding to a flux of $3.0_{-0.7}^{+4.2} \times 10^{-12}$ erg cm $^{-2}$ s $^{-1}$. More recent deep *NuSTAR* observations of the cluster core [55] reported a 20–80 keV flux of $9.5_{-5.5}^{+0.5} \times 10^{-12}$ erg cm $^{-2}$ s $^{-1}$ for a power-law component with $\Gamma = 1.6_{-0.2}^{+0.1}$, although the data were found to favor a multi-temperature thermal model. The brightest point source resolved by *Chandra* contributes only $2.2_{-1.1}^{+1.5} \times 10^{-13}$ erg cm $^{-2}$ s $^{-1}$ in the same band, suggesting that the observed hard X-ray excess is unlikely to be dominated by a single unresolved AGN. Similarly, *Suzaku* observations in the 0.5–40 keV band found that the emission above 10 keV near the cluster center is better explained by a very hot thermal component ($kT > 13$ keV) rather than inverse-Compton emission. No statistically significant non-thermal emission was detected from the northwestern radio relic, yielding a 90% confidence upper limit of 7.3×10^{-13} erg cm $^{-2}$ s $^{-1}$ in the 10–40 keV band [56].

In this work, we present a model for A3667 using the MINOT framework [Modelling and Interpretation of Non-Thermal emission from galaxy clusters Of the milky way Type; 57], a publicly available code designed for self-consistent modelling of non-thermal cluster emission across wavelengths. The MINOT framework has also been used to model the expected non-thermal hadronic gamma-ray and neutrino emission from galaxy clusters. For example, Voitsekhovskiy [58] studied the Hercules cluster (A2151), focusing on the brightest subclumps. Using thermal X-ray observations as inputs to the MINOT code, they simulated the hadronic gamma-ray and neutrino emission produced through cosmic-ray proton interactions in the intracluster medium. Assuming typical cosmic-ray parameters, namely a cosmic-ray-to-thermal energy ratio of $X_{\text{CR,p}} \approx 0.04\text{--}0.06$ and a proton spectral index $\gamma \approx 2.5$, the predicted gamma-ray and neutrino fluxes were found to remain below the sensitivity limits of current and planned instruments. However, the authors showed that additional cosmic-ray injection from AGN activity, mergers, accretion flows, and turbulence could increase the cosmic-ray energy fraction up to $X_{\text{CR,p}} \approx 0.1$ and produce a harder proton spectrum ($\gamma \sim 1.5\text{--}2.0$). Under these conditions, the brighter subclump could become detectable by CTA at the $\sim 5\sigma$ level, while the associated hard-spectrum neutrino emission may also be detectable with next-generation observatories such as IceCube-Gen2. We use the thermal electron density and pressure profiles of A3667 derived from archival *Chandra* X-ray data in the ACCEPT catalog [59], model the magnetic field and cosmic-ray spatial distributions following standard prescriptions, and compute the predicted hadronic and leptonic gamma-ray emission for a range of CR spectral and spatial model assumptions. We compare these predictions with the available multi-instrument observational constraints to assess the consistency of the hadronic model and quantify the relative contribution of hadronic and leptonic emission channels.

This paper is structured as follows. Section II describes the cluster properties, the ACCEPT thermodynamic data, the profile construction methodology, and the MINOT initialization including the non-thermal physics setup. Section III presents the predicted thermodynamic structure, gamma-ray spectra, surface brightness profiles, enclosed fluxes, and IC emission. Section IV compares the predictions with observational constraints from Fermi-LAT [16]. The derived thermodynamic profiles are collected in Appendix A. Throughout this work we adopt a flat Λ CDM cosmology with $H_0 = 67.74$ km s $^{-1}$ Mpc $^{-1}$ and $\Omega_m = 0.3075$ [60].

II. DATA ANALYSIS

A. Cluster Properties and Cosmological Framework

At the cluster redshift, the corresponding angular diameter distance is $D_{\text{ang}} = 230.1$ Mpc. The adopted cluster mass is $M_{500} = 7.16 \times 10^{14} M_{\odot}$, derived from the SPT-SZ catalog [61]. The same Planck 2015 cosmology is used consistently throughout all profile derivations and MINOT modelling steps, following the cosmological framework adopted internally by MINOT [57].

The characteristic radius R_{500} , defined as the radius enclosing a mean density 500 times the critical density of the Universe at the cluster redshift $\rho_c(z)$, is computed as:

$$R_{500} = \left(\frac{3 M_{500}}{4\pi \cdot 500 \cdot \rho_c(z)} \right)^{1/3}, \quad (1)$$

yielding $R_{500} = 1365.5$ kpc. The cluster centre is located at $(\alpha, \delta)_{\text{J2000}} = (303.1763^{\circ}, -56.8432^{\circ})$, as determined from the SPT-SZ catalogue [61]. A truncation radius of $R_{\text{trunc}} = 5000$ kpc $\approx 3.7 R_{500}$ is adopted. A summary of the adopted cluster parameters is provided in Table I.

B. ACCEPT Thermodynamic Data

Thermodynamic profiles of A3667 are obtained from the ACCEPT catalog [59], which provides deprojected, azimuthally averaged radial profiles derived from archival *Chandra* observations. The dataset combines *Chandra*

TABLE I: Adopted global parameters for A3667 used throughout this work.

Parameter	Value	Unit
Redshift z	0.0556	—
$(\alpha, \delta)_{J2000}$	(303.1763, -56.8432)	deg
M_{500}	7.16×10^{14}	M_{\odot}
R_{500}	1365.5	kpc
R_{trunc}	5000	kpc
D_{ang}	230.1	Mpc
H_0	67.74	$\text{km s}^{-1} \text{Mpc}^{-1}$
Ω_m	0.3075	—
$E(z)$	1.0267	—

observations from four observing cycles (ObsIDs 5751, 5752, 5753, and 889), yielding a total cleaned exposure time of ~ 343 ks. We note although this cluster has also been imaged using the eROSITA satellite [62], The eROSITA thermodynamic profiles are not yet publicly available (J. Sanders, private communication) and hence have not been used for this analysis.

The resulting profiles consist of $N = 56$ radial bins spanning 2.7–295.2 kpc, corresponding to 0.002–0.216 R_{500} . Each bin provides the following data:

- **Electron number density** $n_e(r)$ [cm^{-3}], derived from the spectral normalization of a single-temperature APEC plasma model. Across the 56 radial bins the density spans 1.41×10^{-3} to $5.73 \times 10^{-3} \text{ cm}^{-3}$, decreasing outward within the probed radial range.
- **Electron temperature** $T(r)$ [keV], derived from the spectral shape of the APEC model fit. The observed temperature spans 5.08–6.01 keV across the 2.7–295.2 kpc radial range, with a median value of 5.5 keV. The modest radial variation ($\lesssim 16\%$ peak-to-peak) is consistent with the limited radial coverage of the ACCEPT data ($r \lesssim 0.22 R_{500}$).
- **Electron Thermal pressure** $P(r) = n_e k_B T$ [dyne cm^{-2}], converted to keV cm^{-3} via $1 \text{ dyne cm}^{-2} = 6.242 \times 10^8 \text{ keV cm}^{-3}$. The pressure spans 7.54×10^{-3} to $2.91 \times 10^{-2} \text{ keV cm}^{-3}$.

The ACCEPT profiles probe only the cluster core and inner intracluster medium (ICM), extending to $0.216 R_{500}$. Beyond this radius, thermodynamic profiles must be extrapolated using physically motivated parametric models, as described in Section II C. We note that the temperature data are directly used in the construction of the self-consistent pressure profile (cf. Section II C 2).

C. Profile Construction and Extrapolation

The observed thermodynamic profiles are characterized using parametric models and extrapolated to $R_{\text{trunc}} = 5000$ kpc on a logarithmically spaced radial grid of 150 points spanning 1–5500 kpc.

1. Electron Density Profile

The electron density profile is modeled using the standard β -model [63]:

$$n_e(r) = n_0 \left[1 + \left(\frac{r}{r_c} \right)^2 \right]^{-3\beta/2}, \quad (2)$$

with all three parameters — central density n_0 , core radius r_c , and slope β treated as free parameters during the profile fitting procedure. The best-fit parameters, their 1σ uncertainties, and the goodness-of-fit are summarized in Table II. The low $\beta = 0.329$ reflects a shallow outer density gradient. The resulting density profile is shown in Figure 4, where the model is extrapolated from the observed range ($r \lesssim 295$ kpc) to the truncation radius using the best-fit β -model parameters.

2. Thermal Pressure Profile

We construct a pressure profile directly from the fundamental thermodynamic definition:

$$P(r) = n_e(r) k_B T(r), \quad (3)$$

where $n_e(r)$ is given by the best-fit β -model (Section II C 1) and $T(r)$ is derived from the ACCEPT data as $T = P_{\text{ACCEPT}}/n_{e,\text{ACCEPT}}$, then extrapolated using a power-law model:

$$T(r) = T_0 \left(\frac{r}{r_0} \right)^{-\alpha}, \quad (4)$$

with best-fit parameters $T_0 = 5.55$ keV, $r_0 = 158.3$ kpc, and $\alpha = 0.039$ (Table II). At the truncation radius $R_{\text{trunc}} = 5000$ kpc, pressure reaches $P \approx 4 \times 10^{-4}$ keV cm $^{-3}$, confirming that contributions from $r > R_{\text{trunc}}$ are negligible.

TABLE II: Best-fit parameters for the electron density (β -model), and temperature power-law profiles of A3667, derived from *Chandra* ACCEPT data. The Pressure profile adopted for MINOT modelling is computed as $P = n_e \times T$ using the β -model density and the power-law temperature fit.

Profile	Parameter	Value	Unit
β -model (density)	n_0	$(4.49 \pm 0.15) \times 10^{-3}$	cm $^{-3}$
	r_c	95.5 ± 9.6	kpc
	β	0.329 ± 0.019	—
Power-law (temperature)	T_0	5.55	keV
	r_0	158.3	kpc
	α	0.039	—
	T range	5.08–6.01 (data)	keV

D. MINOT Cluster Initialisation and Non-Thermal Physics Setup

The thermodynamic profiles derived in Section II C are ingested into the MINOT framework [57] to construct a complete physical model of A3667 for non-thermal emission modelling. The cluster object is initialized with the parameters summarized in Tables I and II. Three additional physical components must be specified: the magnetic field profile, the cosmic-ray (CR) spatial distribution, and the CR energy spectra. All non-thermal parameters are collected in Table III.

1. Magnetic Field Profile

The ICM magnetic field is assumed to scale with the local thermal electron density as [57, 64] :

$$B(r) = B_0 \left(\frac{n_e(r)}{n_e(r_0)} \right)^{\eta_B}, \quad (5)$$

where $B_0 = 5$ μ G is the field strength at reference radius $r_0 = 100$ kpc and $\eta_B = 0.5$ is the scaling index [65]. With the best-fit β -model density, Eq. (5) yields $B \approx 6.0$ μ G near the cluster centre ($r \sim 1$ kpc), declining to ~ 1.6 μ G at R_{500} and ~ 0.85 μ G at the truncation radius. The radial profile is shown in Figure 2.

2. Cosmic-Ray Spatial Distribution

The number density of both CRp and CRe is scaled with the thermal electron density as:

$$n_{\text{CR}}(r) \propto n_e(r)^{\eta_{\text{CR}}}, \quad (6)$$

with $\eta_{\text{CR}} = 1$ (isodens scaling) adopted as the baseline for both species [30, 57].

Figure 3 compares four spatial models normalized at R_{500} : isodens $\eta = 1$ (baseline), isodens $\eta = 0.5$ (shallower concentration), isobaric ($n_{\text{CR}} \propto P_{\text{gas}}$), and a flat (spatially uniform) profile. The isodens and isobaric models differ by less than 10% within the ACCEPT data range ($r \lesssim 0.22 R_{500}$), owing to the nearly isothermal temperature profile ($\alpha = 0.039$). The flat model diverges most strongly, with $X_{\text{CR}}(r)/X_{\text{CR}}(R_{500})$ rising by a factor of ~ 4 at R_{trunc} relative to the baseline.

The CR content is normalized to R_{500} via:

$$X_{\text{CRp}}(R_{500}) = \left. \frac{\varepsilon_{\text{CRp}}}{\varepsilon_{\text{th}}} \right|_{R_{500}} = 10^{-2}, \quad X_{\text{CRe}}(R_{500}) = \left. \frac{\varepsilon_{\text{CRe}}}{\varepsilon_{\text{th}}} \right|_{R_{500}} = 10^{-5}. \quad (7)$$

These are the fiducial starting values; the sensitivity of predicted observables to X_{CRp} and X_{CRe} is explored in Section III.

3. Cosmic-Ray Energy Spectra

a. Cosmic-ray protons. CRp are modeled with a power-law momentum spectrum:

$$\frac{dN_{\text{CRp}}}{dp} \propto p^{-\alpha_p}, \quad \alpha_p = 2.4. \quad (8)$$

The index $\alpha_p = 2.4$ is consistent with diffusive shock acceleration at merger-driven shock acceleration [$\alpha_p \approx 2-2.5$; 66, 67] and with upper limits from the non-detection of cluster γ -ray emission by Fermi-LAT [14].

b. Primary cosmic-ray electrons. Primary CRe are modelled with a continuous injection spectrum incorporating a cooling break:

$$\frac{dN_{\text{CRe}}}{dE} \propto \begin{cases} E^{-\alpha_e} & E < E_{\text{break}}, \\ E^{-(\alpha_e+1)} & E > E_{\text{break}}, \end{cases} \quad (9)$$

with $\alpha_e = 2.3$, $E_{\text{break}} = 5$ GeV, over $E_e \in [1 \text{ MeV}, 10 \text{ PeV}]$. The index $\alpha_e = 2.3$ is consistent with the integrated spectral index of the A3667 radio relics [42, 43].

c. Secondary cosmic-ray electrons. Secondary CRe from hadronic pp interactions are computed self-consistently by MINOT using the Pythia8 model [68, 69].

d. Electron energy losses and spectral break. The energy loss processes governing the CRe evolution in the A3667 ICM are illustrated in Figure 1. Four mechanisms contribute to $-dE/dt$: synchrotron radiation, IC scattering off CMB photons, bremsstrahlung, and Coulomb collisions [70]. Each process is evaluated at two representative radii — $r = 10$ kpc (inner core) and $r = R_{500} = 1365$ kpc (R_{500}).

At low energies ($E \lesssim 0.1$ GeV), Coulomb losses dominate at both radii, causing electrons to thermalize. The Coulomb rate is proportional to the local electron density and therefore drops by a factor of ~ 14 between $r = 10$ kpc and $r = R_{500}$, reflecting the decline in $n_e(r)$ from 4.5×10^{-3} to $3.2 \times 10^{-4} \text{ cm}^{-3}$. At high energies ($E \gtrsim 1$ GeV), synchrotron and IC losses rise steeply as E^2 , driving efficient radiative cooling.

The relative importance of synchrotron versus IC is set by the local magnetic energy density compared to that of the CMB. The equivalent magnetic field of the CMB at $z = 0.0556$ is $B_{\text{CMB}} = \sqrt{8\pi U_{\text{CMB}}} \approx 3.6 \mu\text{G}$; synchrotron exceeds IC wherever $B(r) > B_{\text{CMB}}$. With the adopted field profile (Eq. 5), this condition holds for $r \lesssim 250$ kpc ($\approx 0.18 R_{500}$). At the inner evaluation radius ($r = 10$ kpc), $B \approx 6.0 \mu\text{G} > B_{\text{CMB}}$ and synchrotron dominates; at $r = R_{500}$, $B \approx 1.6 \mu\text{G} < B_{\text{CMB}}$ and IC losses take over. The two evaluation radii therefore bracket the transition between synchrotron-radiation-dominated and inverse-Compton-dominated cooling, efficiently illustrating both electron cooling regimes within a single figure.

4. Map and Numerical Integration Parameters

The cluster is modeled on a $6^\circ \times 6^\circ$ field of view centered on $(\alpha, \delta) = (303.1763^\circ, -56.8432^\circ)$, with a spatial resolution of 30 arcsec. The truncation radius subtends $\theta_{\text{trunc}} = 1.245^\circ$ and the characteristic cluster radius subtends $\theta_{500} = 0.340^\circ$, both comfortably within the field of view.

The volume integrals are evaluated on a logarithmic radial grid with 50 points per decade between $R_{\text{min}} = 1$ kpc and $R_{\text{trunc}} = 5000$ kpc, providing adequate sampling over four decades in radius. EBL absorption of γ -ray emission is modeled using the models in Domínguez et al. [71].

III. RESULTS

A. Thermodynamic Structure of A3667

Using the MINOT cluster model constructed in Section II, we derive the full thermodynamic structure of A3667 from 1 kpc to the truncation radius $R_{\text{trunc}} = 5000$ kpc $\approx 3.7 R_{500}$. The results are presented in Figures 4, 5, and 6.

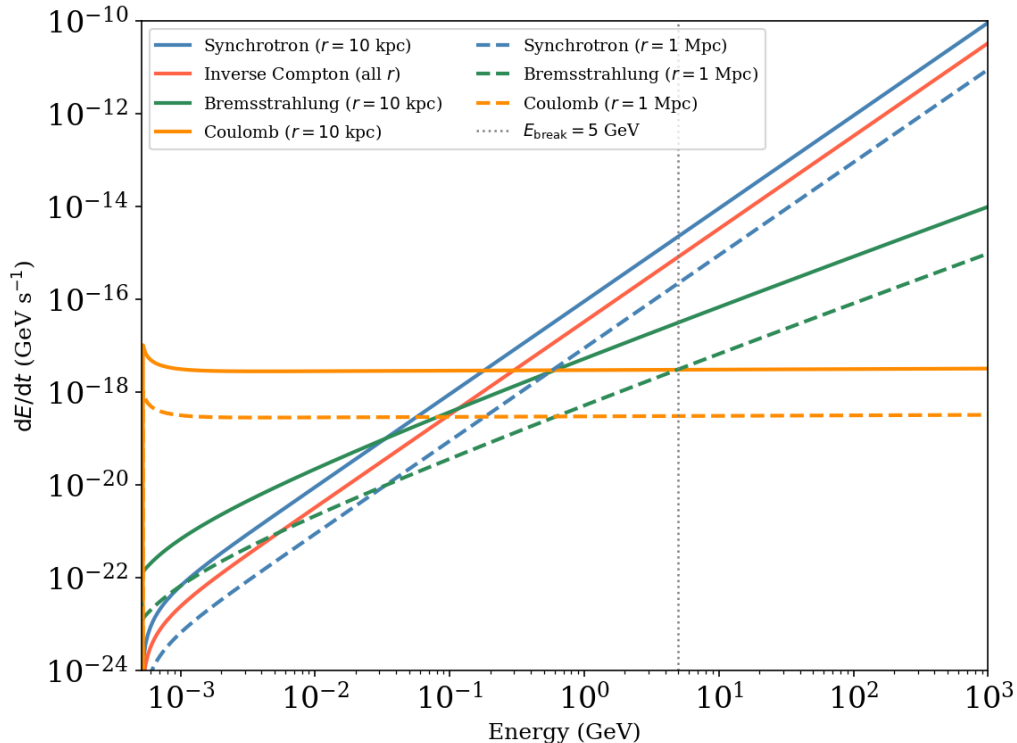


FIG. 1: Electron energy loss rates in the A3667 ICM as a function of electron energy, evaluated at $r = 10$ kpc (solid lines) and $r = R_{500} = 1365$ kpc (dashed lines). Four loss mechanisms are shown: synchrotron (blue), IC (red; single curve, identical at all radii as it depends only on the CMB radiation field at $z = 0.0556$), bremsstrahlung (green), and Coulomb (orange). The vertical dotted line marks the spectral break energy $E_{\text{break}} = 5$ GeV. At $r = 10$ kpc, $B \approx 6.0 \mu\text{G} > B_{\text{CMB}} \approx 3.6 \mu\text{G}$, so synchrotron dominates IC; at $r = R_{500}$, $B \approx 1.6 \mu\text{G} < B_{\text{CMB}}$ and IC dominates. Coulomb losses control the sub-0.1 GeV behavior at both radii. The break energy lies within the radiative regime at all cluster radii, justifying the Continuous Injection spectral model adopted for the primary CRE.

1. Electron Density

The electron density profile, shown in Figure 4, is described by the best-fit β -model with parameters $n_0 = 4.49 \times 10^{-3} \text{ cm}^{-3}$, $r_c = 95.5$ kpc, and $\beta = 0.329$. The profile exhibits a flat, nearly constant core within $r \lesssim 20$ kpc, followed by a power-law decline at larger radii. At R_{500} the density has declined to $n_e(R_{500}) = 3.11 \times 10^{-4} \text{ cm}^{-3}$. The profile reaches $n_e \approx 8 \times 10^{-5} \text{ cm}^{-3}$ at the radius of truncation.

2. Thermal Pressure

The pressure profile $P(r) = n_e(r) \times T(r)$, shown in Figure 5, decreases from $P \approx 3.03 \times 10^{-2} \text{ keV cm}^{-3}$ in the cluster core to $P(R_{500}) = 1.59 \times 10^{-3} \text{ keV cm}^{-3}$, reaching $P \approx 4 \times 10^{-4} \text{ keV cm}^{-3}$ in the truncation radius.

3. Temperature

The temperature profile, shown in Figure 6, is nearly isothermal across the full radial range, consistent with the power-law fit $T(r) = T_0 (r/r_0)^{-\alpha}$ with $\alpha = 0.039$. The temperature declines only modestly from $T \approx 5.9$ keV at $r = 10$ kpc to $T(R_{500}) = 5.09$ keV at R_{500} .

B. Predicted Gamma-ray Emission from Hadronic Interactions

We compute the gamma-ray emission from A3667 arising from hadronic cosmic-ray proton interactions with the thermal ICM via inelastic proton-proton (pp) collisions:

TABLE III: Non-thermal model parameters adopted for the MINOT initialization of A3667.

Parameter	Value	Unit
<i>Magnetic field</i>		
B_0	5.0	μG
r_0	100	kpc
η_B	0.5	—
$B(r\sim 0)$	≈ 6.0	μG
$B(R_{500})$	≈ 1.6	μG
$B(R_{\text{trunc}})$	≈ 0.85	μG
<i>Cosmic-ray protons</i>		
Spectrum	PowerLaw	—
α_p	2.4	—
X_{CRp}	10^{-2}	—
$E_{p,\text{min}}$	1.22	GeV
$E_{p,\text{max}}$	10	PeV
<i>Cosmic-ray electrons</i>		
Spectrum	ContinuousInjection	—
α_e	2.3	—
E_{break}	5	GeV
X_{CRe}	10^{-5}	—
$E_{e,\text{min}}$	1	MeV
$E_{e,\text{max}}$	10	PeV
<i>Spatial distribution (both species)</i>		
Model	Isodens ($\eta_{\text{CR}} = 1$)	—
<i>Map and integration</i>		
Field of view	6×6	deg
Resolution	30	arcsec
θ_{500}	0.340	deg
θ_{trunc}	1.245	deg
EBL model	Domínguez et al. [71]	—

$$p + p \rightarrow p + p + \pi^0 + \dots, \quad \pi^0 \rightarrow \gamma + \gamma. \quad (10)$$

The resulting gamma-ray flux depends on the spatial distribution and energy spectrum of the CRp population, the thermal gas density, and the cluster volume. All calculations are performed using the MINOT framework with the Pythia8 hadronic interaction model [57], using the baseline cluster model described in Section IID. We additionally compute the contribution from IC scattering of primary CRe off CMB photons as a reference channel.

1. Gamma-ray Spectrum

Figure 7 shows the predicted gamma-ray spectral energy distribution (SED) $E^2 dN/dE dS dt$ as a function of photon energy, integrated over the full cluster volume out to $R_{\text{trunc}} = 5000$ kpc. The baseline hadronic spectrum (solid blue; $\alpha_p = 2.4$, isodens scaling $\eta = 1$) exhibits the broad spectral bump characteristic of neutral pion decay, with maximum power emitted near $E_\gamma \sim 1$ GeV and strong suppression above $E_\gamma \sim 10^4$ GeV. The effect of varying the CRp spectral index is shown by the dashed ($\alpha_p = 2.1$) and dotted ($\alpha_p = 2.8$) blue curves. A harder CRp spectrum ($\alpha_p = 2.1$) shifts the gamma-ray power toward higher energies and enhances the TeV emission, whereas a softer spectrum ($\alpha_p = 2.8$) suppresses the high-energy tail and concentrates the emission near the GeV peak. The predicted flux varies by approximately one order of magnitude across this range of spectral indices within the Fermi-LAT energy band, highlighting the strong sensitivity of the gamma-ray emission to the CRp spectral slope.

The dash-dotted curve shows the effect of reducing the CRp spatial concentration to $\eta = 0.5$ (i.e. $n_{\text{CRp}} \propto n_e^{0.5}$ rather than n_e). This produces an approximate $\sim 30\%$ reduction in the total flux while preserving the spectral shape, demonstrating that the spatial distribution of CRp primarily affects the emission normalization rather than the spectral slope. The IC contribution from primary CRe (gray dashed) remains subdominant across the full energy range, typically lying one to two orders of magnitude below the hadronic component. This confirms that the predicted gamma-ray emission from A3667 is dominated by hadronic processes for the assumed CR normalizations.

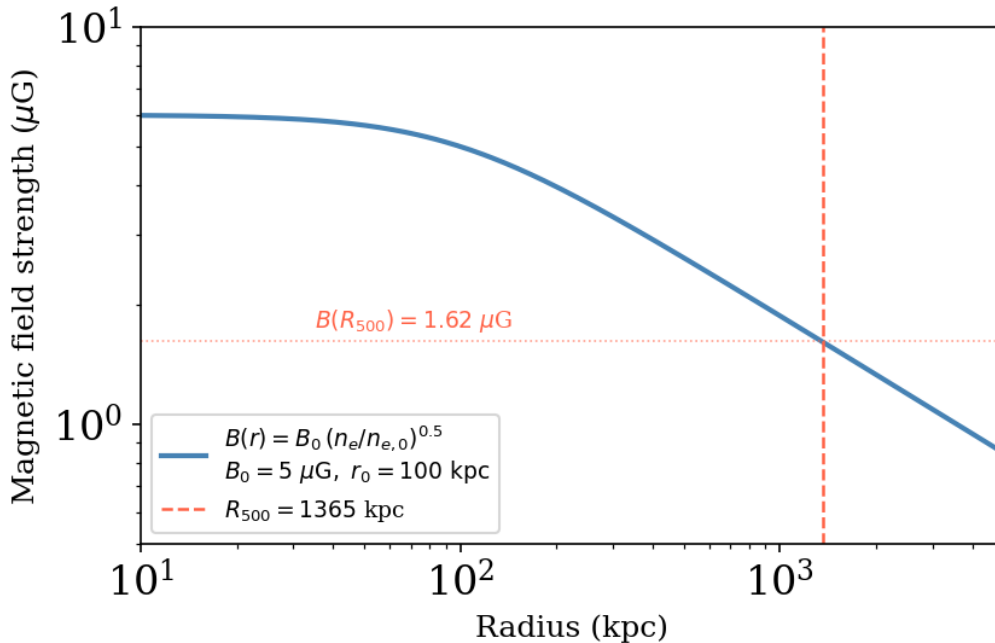


FIG. 2: Magnetic field strength profile of A3667 from Eq. (5) with $B_0 = 5 \mu\text{G}$, $\eta_B = 0.5$, and $r_0 = 100 \text{ kpc}$. The field declines from $\approx 6 \mu\text{G}$ near the center to $\approx 1.6 \mu\text{G}$ at R_{500} (red dashed) and $\approx 0.85 \mu\text{G}$ at R_{trunc} . The annotated value at R_{500} is marked for reference.

2. Enclosed Gamma-ray Flux

Figure 8 shows the enclosed gamma-ray flux $F(< r)$ as a function of aperture radius, integrated over 500 MeV–1 TeV using spherical integration. The flux increases monotonically with radius, reflecting the extended nature of the cluster emission. At $R_{500} = 1365 \text{ kpc}$, the enclosed flux is $F(< R_{500}) = 6.45 \times 10^{-11} \text{ cm}^{-2} \text{ s}^{-1}$, which represents only $\sim 24\%$ of the total flux within the truncation radius $F(< R_{\text{trunc}}) = 2.63 \times 10^{-10} \text{ cm}^{-2} \text{ s}^{-1}$. The remaining $\sim 76\%$ of the gamma-ray emission originates from beyond R_{500} , a consequence of the shallow outer density profile ($\beta = 0.329$) which sustains a significant gas column to large radii.

The predicted flux values across all computed energy bands are summarised in Table IV. In the Fermi-LAT band (1–300 GeV), the predicted flux within R_{500} is $F(< R_{500}) = 2.82 \times 10^{-11} \text{ cm}^{-2} \text{ s}^{-1}$, rising to $1.15 \times 10^{-10} \text{ cm}^{-2} \text{ s}^{-1}$ within the truncation radius. For the broader 500 MeV–1 TeV energy range, the corresponding fluxes increase to $6.45 \times 10^{-11} \text{ cm}^{-2} \text{ s}^{-1}$ within R_{500} and $2.63 \times 10^{-10} \text{ cm}^{-2} \text{ s}^{-1}$ within R_{trunc} . The integrated broad-band flux over 100 MeV–100 TeV reaches $2.18 \times 10^{-10} \text{ cm}^{-2} \text{ s}^{-1}$ and $8.89 \times 10^{-10} \text{ cm}^{-2} \text{ s}^{-1}$ within R_{500} and R_{trunc} , respectively. In all energy bands, the total flux increases by a factor of approximately four between R_{500} and R_{trunc} , indicating that a substantial fraction of the predicted gamma-ray emission originates from the extended cluster outskirts. These values are computed for the baseline hadronic model with $X_{\text{CRp}} = 10^{-2}$ and $\alpha_p = 2.4$, and scale linearly with the assumed CRp normalization.

TABLE IV: Predicted gamma-ray flux from A3667 for the baseline hadronic model ($\alpha_p = 2.4$, $\eta = 1$, $X_{\text{CRp}} = 10^{-2}$) across three energy bands, computed using spherical integration. Fluxes scale linearly with X_{CRp} .

Energy band	$F(< R_{500})$ ($\text{cm}^{-2} \text{ s}^{-1}$)	$F(< R_{\text{trunc}})$ ($\text{cm}^{-2} \text{ s}^{-1}$)
500 MeV–1 TeV	6.45×10^{-11}	2.63×10^{-10}
1–300 GeV (Fermi-LAT)	2.82×10^{-11}	1.15×10^{-10}
100 MeV–100 TeV (broad)	2.18×10^{-10}	8.89×10^{-10}

3. Gamma-ray Surface Brightness Map

Figure 9 shows the two-dimensional gamma-ray surface brightness map of A3667 in the 500 MeV–1 TeV band. The emission is circularly symmetric and centrally concentrated, peaking at the cluster center with a surface

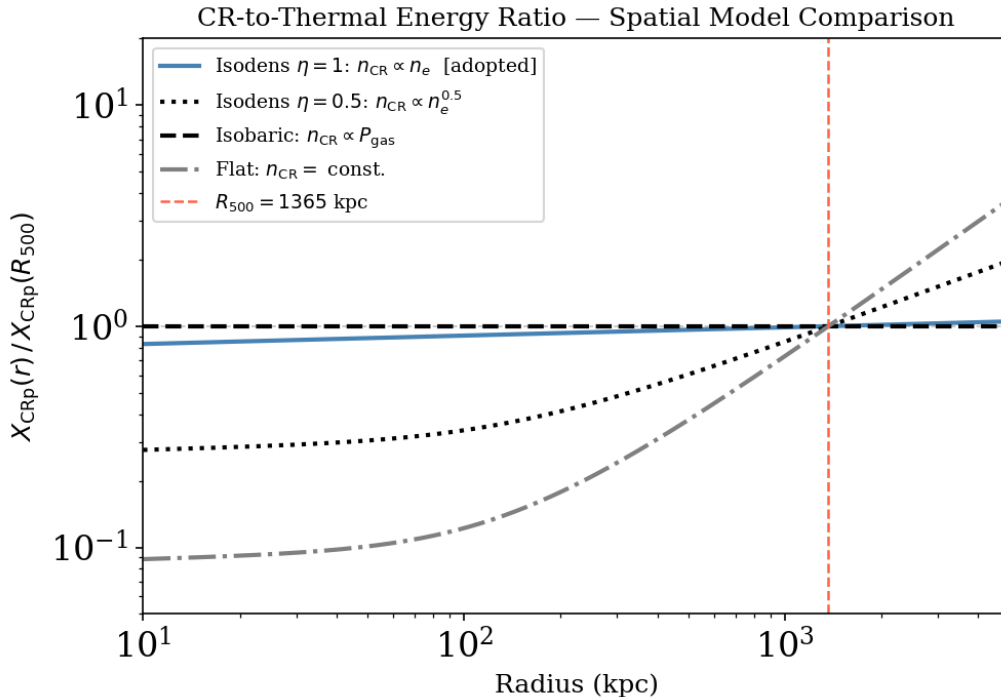


FIG. 3: Normalized CR-to-thermal energy ratio $X_{\text{CRp}}(r)/X_{\text{CRp}}(R_{500})$ under four spatial models: isodens $\eta = 1$ (solid blue, adopted baseline), isodens $\eta = 0.5$ (dotted), isobaric (dashed), and flat (dot-dashed grey). All curves are normalized to unity at R_{500} (red dashed line). The four models differ by less than 10% within the data range; they diverge significantly only in the extrapolated regime.

brightness of $\sim 10^{-5.5} \text{ cm}^{-2} \text{ s}^{-1} \text{ sr}^{-1}$ and declining to $\sim 10^{-8.5} \text{ cm}^{-2} \text{ s}^{-1} \text{ sr}^{-1}$ at the cluster outskirts, spanning a dynamic range of three orders of magnitude. The circular symmetry reflects the azimuthally averaged nature of the input thermodynamic profiles; in reality, the merging morphology of A3667 with its prominent cold fronts and radio relics would produce significant asymmetries in the actual CR and gas distributions not captured by our spherically symmetric model.

The red dashed circle marks $R_{500} = 1365 \text{ kpc}$, corresponding to an angular radius of $\theta_{500} = 0.340^\circ$ at the cluster redshift. The brightest emission is strongly concentrated within R_{500} , although as shown in Figure 8 the integrated flux is dominated by the extended emission beyond this radius.

C. Predicted IC Emission from Cosmic-Ray Electrons

We compute the predicted gamma-ray emission from A3667 arising from IC scattering of cosmic-ray electrons (CRE) off the cosmic microwave background (CMB) radiation field. We separately treat two CRE populations: *primary* electrons injected directly by acceleration processes at merger shocks and turbulence, and *secondary* electrons produced as decay products of charged pions from hadronic pp interactions. All calculations are performed using the MINOT framework with the baseline cluster model described in Section IID, using an energy grid spanning 10^{-6} – 10^4 GeV over the radial range 1–5000 kpc. We additionally compute the total IC emission (primary plus secondary) across three energy bands and compare with the hadronic pion-decay predictions of Section IIIB.

1. IC Spectrum

Figure 10 shows the predicted IC spectral energy distribution (SED) $E^2 dN/dE dS dt$ as a function of photon energy, integrated over the full cluster volume out to $R_{\text{trunc}} = 5000 \text{ kpc}$.

The primary CRE component (solid blue) and secondary CRE component (solid red) are shown separately, with their sum given by the total IC curve (solid black). The secondary IC emission arises from the same hadronic CRp population that drives the pion-decay channel discussed in Section IIIB. For the baseline parameters ($X_{\text{CRp}} = 10^{-2}$, $\alpha_p = 2.4$, $\eta = 1$), the secondary IC flux is subdominant to the primary CRE contribution across

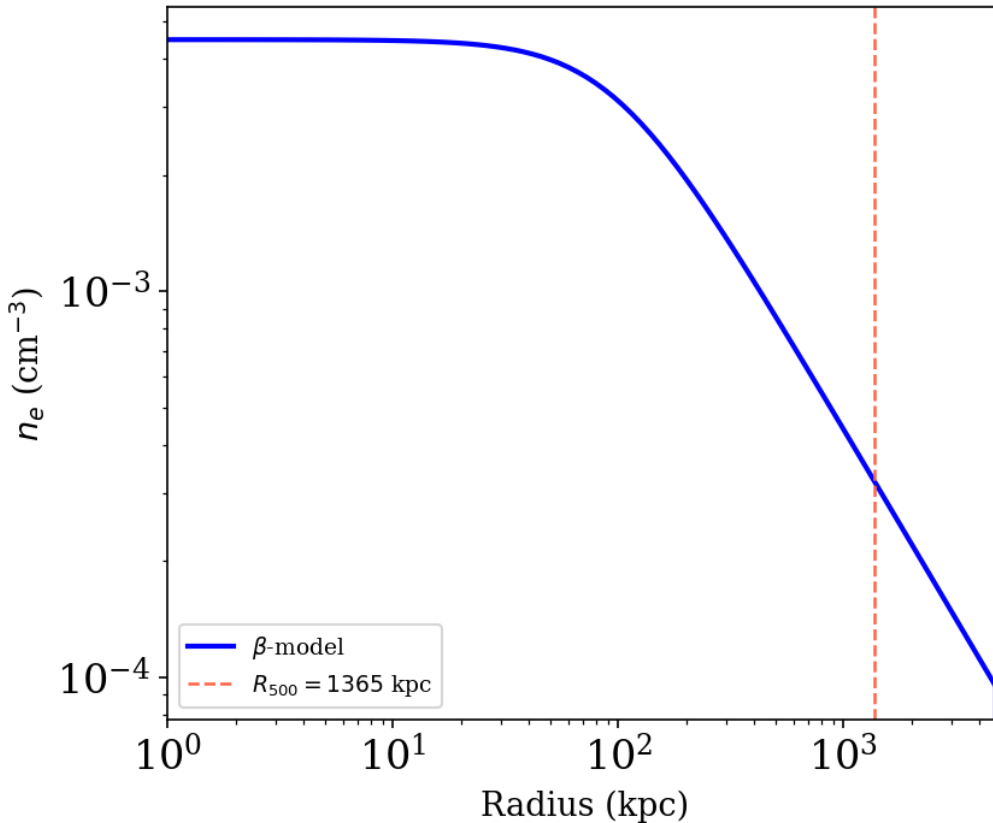


FIG. 4: Electron density profile of A3667 derived from the best-fit β -model. The solid blue curve shows the model extrapolated from the observed radial range ($r \lesssim 295$ kpc) to $R_{\text{trunc}} = 5000$ kpc using the best-fit β -model parameters. The red dashed line marks the R_{500} value.

most of the energy range.

The dashed blue curve shows the `InitialInjection` CRe spectral model, which corresponds to a cooled electron population and exhibits a characteristic steepening. The dotted blue curve shows a pure power-law CRe spectrum with $X_{\text{CRe}} = 10^{-2}$ and spectral index one unit steeper than the baseline. The dependence of the secondary IC emission on CRp parameters mirrors the behavior seen in the hadronic channel. The red dashed ($\alpha_p = 2.8$) and red dash-dotted ($\alpha_p = 2.1$) red curves show that harder CRp spectra produce higher secondary IC fluxes at all energies, while the dotted red curve ($n_{\text{CRp}} \propto n_e^{0.5}$, $\eta = 0.5$) demonstrates a modest reduction in normalization from the shallower CRp spatial profile, with no change to the spectral shape. Across all model variations, the IC SED peaks at sub-GeV energies and falls steeply above ~ 1 GeV, in contrast to the characteristic peaked pion-decay spectrum of the hadronic channel.

2. Enclosed IC Flux

Figure 11 shows the enclosed IC flux $F_{\text{IC}}(< r)$ as a function of aperture radius, integrated over 500 MeV–1 TeV using spherical integration. The flux increases monotonically with radius and has not converged by R_{500} , consistent with the extended nature of the CRe distribution. The predicted IC flux values across all computed energy bands are summarised in Table V.

At $R_{500} = 1365$ kpc, the enclosed IC flux is $F_{\text{IC}}(< R_{500}) = 3.07 \times 10^{-12} \text{ cm}^{-2} \text{ s}^{-1}$, rising to $F_{\text{IC}}(< R_{\text{trunc}}) = 3.33 \times 10^{-11} \text{ cm}^{-2} \text{ s}^{-1}$ within the truncation radius. The ratio of flux within R_{500} to flux within R_{trunc} is $\sim 9\%$, meaning that $\sim 91\%$ of the total IC emission originates from beyond R_{500} . This is even more extreme than in the hadronic case ($\sim 76\%$ beyond R_{500}).

Comparing the IC and hadronic flux predictions directly, the IC contribution within R_{500} is lower than the hadronic value by a factor of ~ 21 in the main 500 MeV–1 TeV band, and by a factor of ~ 21 in the Fermi-LAT band (1–300 GeV; $F_{\text{IC}}(< R_{500}) = 1.37 \times 10^{-12} \text{ cm}^{-2} \text{ s}^{-1}$), consistent with the two-orders-of-magnitude subdominance noted in the spectral comparison of Section III B 1. Within the truncation radius the ratio narrows to a factor of ~ 8 owing to the greater spatial extension of the IC emission, but the hadronic channel

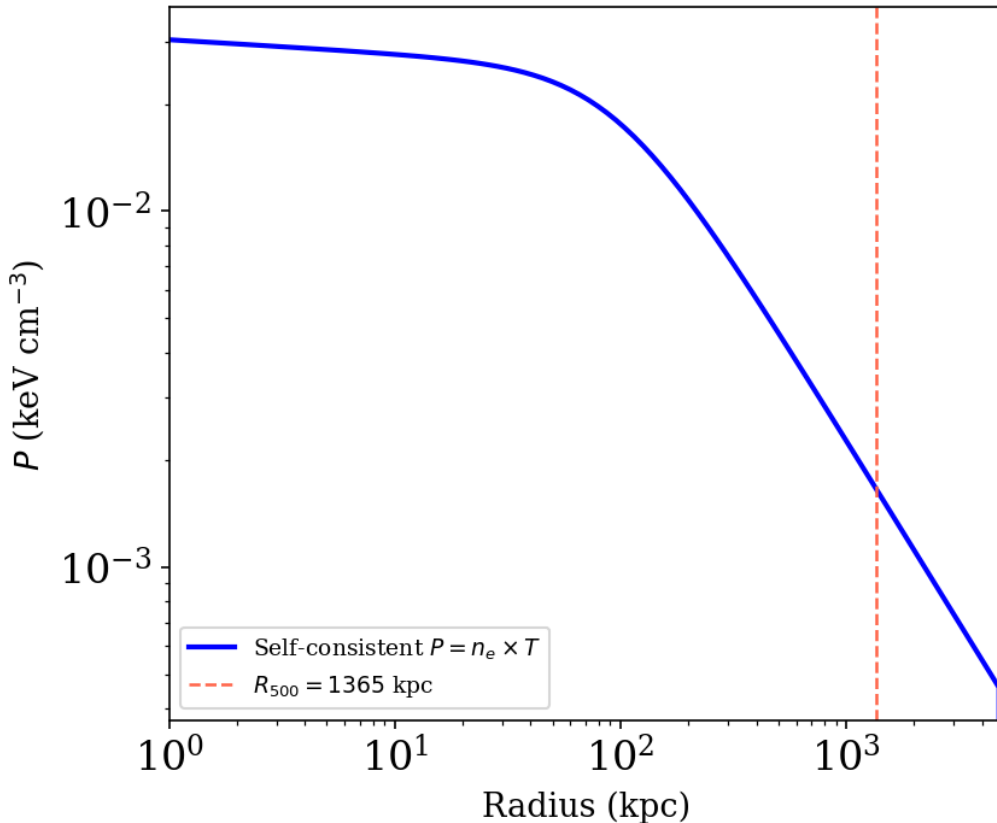


FIG. 5: The thermal pressure profile of A3667 derived from the self-consistent relation $P = n_e \times T$. The profile is extrapolated from the observed radial range ($r \lesssim 295$ kpc) to the truncation radius using the best-fit β -model parameters. The red dashed line marks the R_{500} value.

remains dominant at all apertures for the assumed CR normalizations.

The IC emission from A3667 is subdominant to the hadronic channel by a factor of ~ 21 within R_{500} and ~ 8 within R_{trunc} in the Fermi-LAT band, confirming that the predicted gamma-ray signal from A3667 is of hadronic origin for the assumed CR normalizations. The reported Fermi-LAT flux of $1.3 \times 10^{-10} \text{ cm}^{-2} \text{ s}^{-1}$ [16] is reproduced in order of magnitude by the hadronic model integrated to R_{trunc} ($1.15 \times 10^{-10} \text{ cm}^{-2} \text{ s}^{-1}$), while the total IC flux at the same aperture reaches only $1.49 \times 10^{-11} \text{ cm}^{-2} \text{ s}^{-1}$, an order of magnitude below both the hadronic prediction and the observation. Any gamma-ray signal from A3667 at Fermi-LAT energies is therefore hadronic in origin; the IC channel cannot account for the observed emission even if the primary CRE normalization is raised by an order of magnitude. Independent detection of the IC component would require next-generation MeV instruments with sensitivity in the sub-GeV regime where the IC SED peaks, such as AMEGO-X [72].

TABLE V: Predicted IC flux from A3667 for the baseline model ($\alpha_p = 2.4$, $\eta = 1$, $X_{\text{CRp}} = 10^{-2}$) across three energy bands, from spherical integration. Both primary and secondary CRE contributions are included. Fluxes scale linearly with X_{CRp} for the secondary component.

Energy band	$F_{\text{IC}}(< R_{500})$ ($\text{cm}^{-2} \text{ s}^{-1}$)	$F_{\text{IC}}(< R_{\text{trunc}})$ ($\text{cm}^{-2} \text{ s}^{-1}$)
500 MeV–1 TeV	3.07×10^{-12}	3.33×10^{-11}
1–300 GeV (Fermi-LAT)	1.37×10^{-12}	1.49×10^{-11}
100 MeV–100 TeV (broad)	1.97×10^{-11}	2.14×10^{-10}

3. IC Surface Brightness Map

Figure 12 shows the two-dimensional IC surface brightness map of A3667 in the 500 MeV–1 TeV band. The map is clipped to $\pm R_{\text{trunc}}$ in both axes and displayed on a logarithmic colour scale.

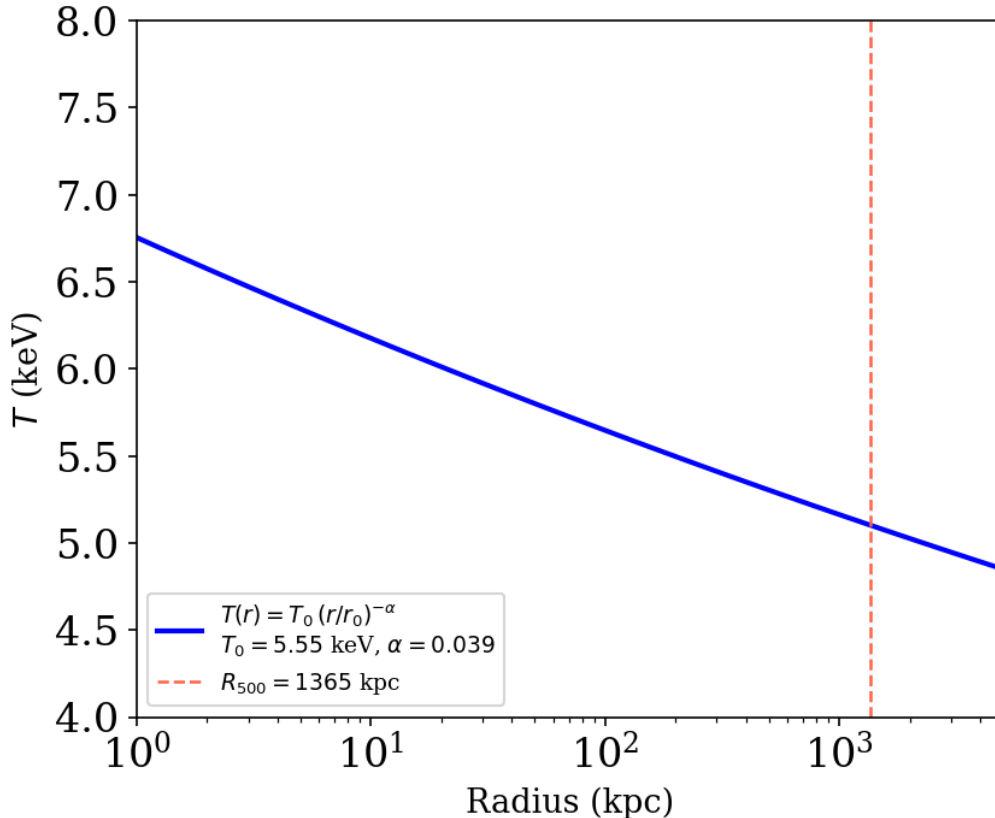


FIG. 6: Temperature profile of A3667 derived from the power-law fit $T(r) = T_0 (r/r_0)^{-\alpha}$. The best-fit model is extrapolated from the observed radial range ($r \lesssim 295$ kpc) to the truncation radius using the fitted parameters. The red dashed line marks the R_{500} value.

The IC emission is circularly symmetric and spatially extended, with a shallower central concentration and a broader morphology than the hadronic pion-decay map of Section III B 3. The peak surface brightness at the cluster center is lower than in the hadronic case.

The red dashed circle marks $R_{500} = 1365$ kpc, corresponding to an angular radius of $\theta_{500} = 0.340^\circ$ at the cluster redshift. The IC emission fills and extends well beyond this circle, in contrast to the hadronic map where the brightest emission is tightly concentrated within R_{500} , even though both channels contribute the majority of their integrated flux from beyond R_{500} (see Sections III B 2 and III C 2).

As with the hadronic map, the circular symmetry of the IC emission reflects the azimuthally averaged input profiles; the true IC morphology in A3667 would be influenced by the actual CRe transport, energy loss history, and the asymmetric gas distribution associated with this merging system. These effects are not captured by our spherically symmetric model.

IV. COMPARISON WITH OBSERVATIONAL CONSTRAINTS

We compare the predicted gamma-ray flux from both the hadronic pion-decay model (Section III B) and the IC model (Section III C) with existing observational constraints from Fermi-LAT [16] across computed energy bands.

a. Fermi-LAT Flux A gamma-ray signal from A3667 has been reported in the 1–300 GeV energy range using Fermi-LAT data, with an estimated photon flux of approximately $1.3 \times 10^{-10} \text{ cm}^{-2} \text{ s}^{-1}$, with a best-fit spectral index of $\Gamma = -3.61 \pm 0.33$ [16]. In the Fermi-LAT band (1–300 GeV), our predicted hadronic photon flux integrated within R_{500} is $F_{\text{had}}(< R_{500}) = 2.82 \times 10^{-11} \text{ cm}^{-2} \text{ s}^{-1}$, which is of order $\mathcal{O}(10^{-11}) \text{ cm}^{-2} \text{ s}^{-1}$, one order of magnitude below the observed value of $\mathcal{O}(10^{-10}) \text{ cm}^{-2} \text{ s}^{-1}$. When the integration is extended to the truncation radius, the predicted flux rises to $F_{\text{had}}(< R_{\text{trunc}}) = 1.15 \times 10^{-10} \text{ cm}^{-2} \text{ s}^{-1}$, of order $\mathcal{O}(10^{-10}) \text{ cm}^{-2} \text{ s}^{-1}$, in order-of-magnitude agreement with the observed value.

A separate analysis by Li and Han [18] also reported a possible gamma-ray excess near the cluster center with $\text{TS} \sim 24.3$ and an integral photon flux of $(2.93 \pm 0.69) \times 10^{-10} \text{ ph cm}^{-2} \text{ s}^{-1}$ in the 0.5–500 GeV energy

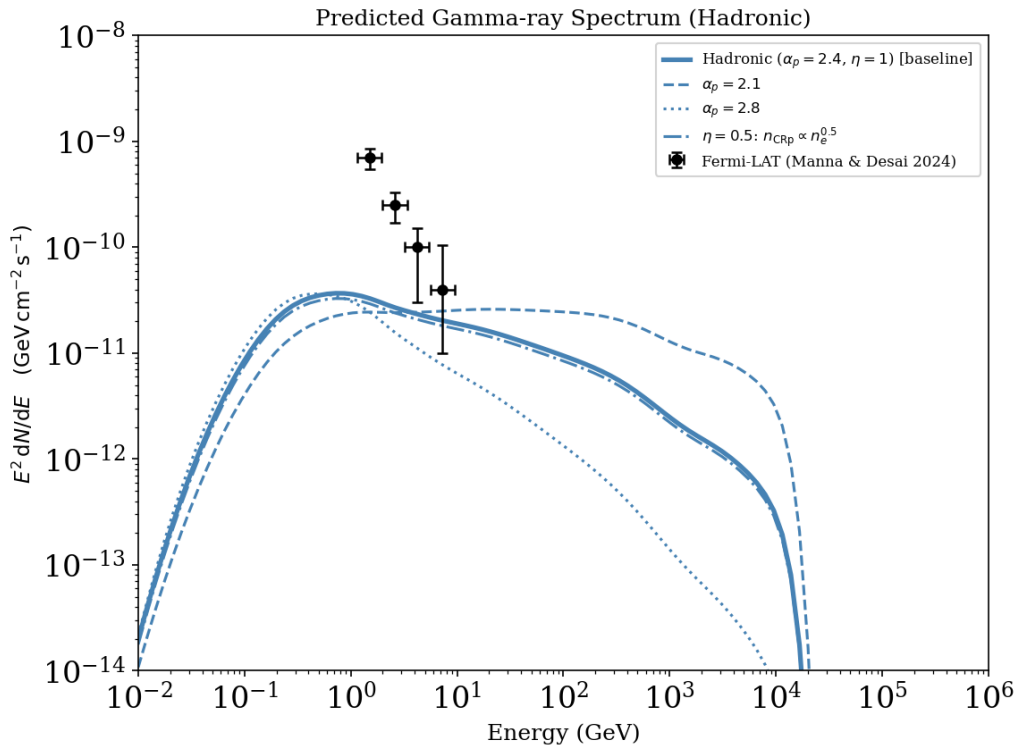


FIG. 7: Predicted gamma-ray spectral energy distribution of A3667 from hadronic pp interactions, integrated over the full cluster volume to R_{trunc} . The solid blue curve shows the baseline model ($\alpha_p = 2.4$, isodens $\eta = 1$, $X_{\text{CRp}} = 10^{-2}$). Dashed and dotted blue curves show spectral index variations $\alpha_p = 2.1$ and 2.8 respectively. The dash-dotted blue curve shows the effect of a shallower CRp spatial profile ($\eta = 0.5$, $n_{\text{CRp}} \propto n_e^{0.5}$). Black flux points show the Fermi-LAT spectral flux measurements of A3667 from Manna and Desai [16], spanning the 1–10 GeV energy range.

range. However, the authors noted that the detected emission may be associated with nearby radio sources, and therefore the cluster origin of the gamma-ray signal remains uncertain.

This suggests that the Fermi-LAT observed flux is better reproduced by the flux computed out to R_{trunc} rather than R_{500} alone. However, this agreement in flux must be interpreted with caution. The observed spectral index $\Gamma = -3.61 \pm 0.33$ is substantially softer than the hadronic prediction of $\Gamma_{\text{had}} \approx -2.4$ to -2.6 expected for $\alpha_p = 2.4$ in this energy range. Even our softest hadronic model with $\alpha_p = 2.8$ does not reproduce a spectral slope as steep as $\Gamma = -3.61$, suggesting that a pure hadronic ICM model with standard isobaric CRp cannot fully account for the observed spectral shape, and that background contamination may contribute to the reported signal.

The predicted IC flux in the Fermi-LAT band (1–300 GeV) is $F_{\text{IC}}(< R_{500}) = 1.37 \times 10^{-12} \text{ cm}^{-2} \text{ s}^{-1}$, of order $\mathcal{O}(10^{-12}) \text{ cm}^{-2} \text{ s}^{-1}$, which is two orders of magnitude below the observed value of $\mathcal{O}(10^{-10}) \text{ cm}^{-2} \text{ s}^{-1}$. Even extending the integration to the truncation radius, the IC flux rises only to $F_{\text{IC}}(< R_{\text{trunc}}) = 1.49 \times 10^{-11} \text{ cm}^{-2} \text{ s}^{-1}$, of order $\mathcal{O}(10^{-11}) \text{ cm}^{-2} \text{ s}^{-1}$, still one order of magnitude below the observation. In both cases, the IC flux is also substantially below the predicted hadronic flux in the same band ($\mathcal{O}(10^{-11})$ – $\mathcal{O}(10^{-10}) \text{ cm}^{-2} \text{ s}^{-1}$), confirming that the IC channel makes a negligible contribution to any detectable signal in the Fermi-LAT band. If the observed emission is real, it is therefore hadronic in origin rather than IC.

b. Band-by-band comparison. Across all three energy bands, the hadronic emission dominates the IC contribution. In the 500 MeV–1 TeV band, the hadronic flux is $\mathcal{O}(10^{-11}) \text{ cm}^{-2} \text{ s}^{-1}$ within R_{500} and $\mathcal{O}(10^{-10}) \text{ cm}^{-2} \text{ s}^{-1}$ within R_{trunc} , while the IC flux is $\mathcal{O}(10^{-12})$ and $\mathcal{O}(10^{-11}) \text{ cm}^{-2} \text{ s}^{-1}$ respectively, giving hadronic-to-IC ratios of ~ 21 within R_{500} and ~ 8 within R_{trunc} . In the Fermi-LAT band (1–300 GeV), the hadronic flux is $\mathcal{O}(10^{-11}) \text{ cm}^{-2} \text{ s}^{-1}$ within R_{500} and $\mathcal{O}(10^{-10}) \text{ cm}^{-2} \text{ s}^{-1}$ within R_{trunc} , with the IC flux one further order of magnitude below the hadronic at both apertures, giving a ratio of ~ 21 within R_{500} and ~ 8 within R_{trunc} . In the broad band (100 MeV–100 TeV), both hadronic and IC fluxes reach $\mathcal{O}(10^{-10}) \text{ cm}^{-2} \text{ s}^{-1}$ at R_{trunc} , with the hadronic flux exceeding the IC by a factor of ~ 11 within R_{500} and ~ 4 within R_{trunc} , where the greater spatial extension of the IC emission becomes more competitive at large apertures.

Regarding observational constraints, the Fermi-LAT observed flux of $\mathcal{O}(10^{-10}) \text{ cm}^{-2} \text{ s}^{-1}$ is reproduced at the same order by the hadronic model integrated to R_{trunc} , while the flux within R_{500} alone falls one order of magnitude short at $\mathcal{O}(10^{-11}) \text{ cm}^{-2} \text{ s}^{-1}$.

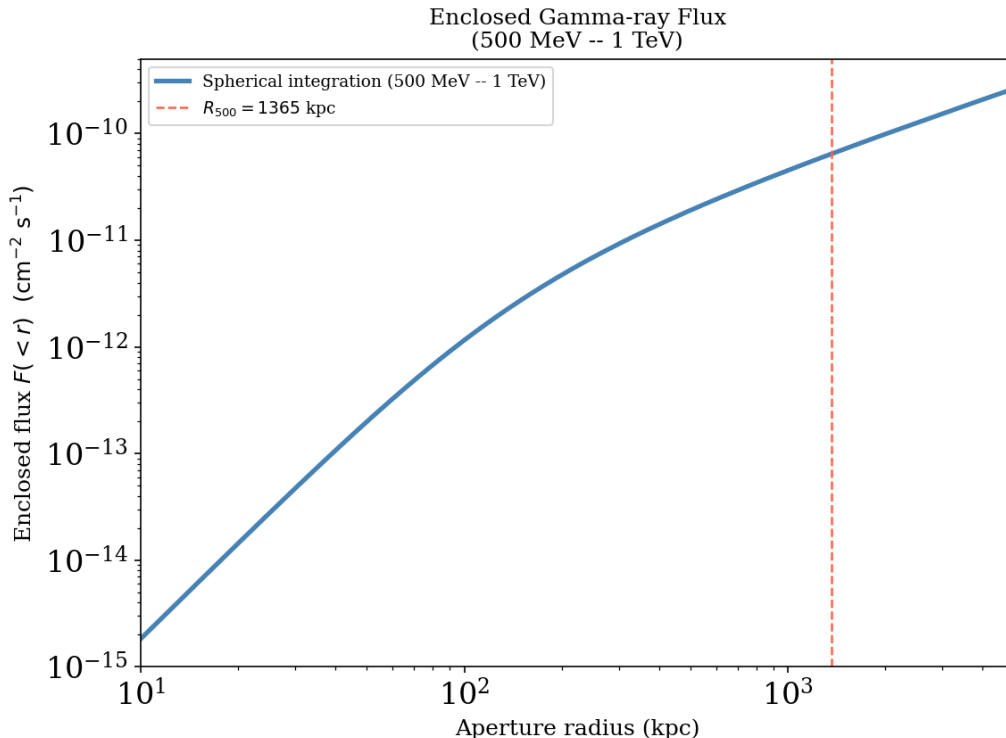


FIG. 8: Enclosed gamma-ray flux $F(<r)$ as a function of aperture radius for A3667 in the 500 MeV–1 TeV band (spherical integration). The flux continues to rise beyond R_{500} (red dashed), with $\sim 76\%$ of the total flux originating from $r > R_{500}$, reflecting the shallow outer density profile of this merging cluster.

V. CONCLUSIONS AND DISCUSSIONS

Motivated by the recent detection of a gamma-ray signal from A3667, we have used the MINOT framework [57], combining archival *Chandra* X-ray data [59] with hadronic and leptonic cosmic-ray emission models in order to calculate the expected gamma-ray flux and spectrum. Our main findings are as follows:

1. *Hadronic gamma-ray emission.* The predicted hadronic gamma-ray flux in the 1–300 GeV band is $F_{\text{had}}(< R_{500}) = 2.82 \times 10^{-11} \text{ cm}^{-2} \text{ s}^{-1}$ within R_{500} , rising to $F_{\text{had}}(< R_{\text{trunc}}) = 1.15 \times 10^{-10} \text{ cm}^{-2} \text{ s}^{-1}$ at the truncation radius. The latter is in order-of-magnitude agreement with the Fermi-LAT reported flux of $1.3 \times 10^{-10} \text{ cm}^{-2} \text{ s}^{-1}$ [16]. Approximately 76% of the total hadronic flux originates from beyond R_{500} .
2. *IC emission subdominant.* The IC contribution from primary and secondary CRE is subdominant by a factor of ~ 21 relative to the hadronic channel within R_{500} in the Fermi-LAT band, and remains below the hadronic flux at all apertures and energy bands considered. The IC emission is more spatially extended than the hadronic component ($\sim 91\%$ of IC flux from $r > R_{500}$ compared to $\sim 76\%$ for hadronic), but is not independently detectable at current instrument sensitivities.
3. *Consistency with observational upper limits.* The hadronic model at $X_{\text{CRp}} = 10^{-2}$ satisfies all available upper limits from DAMPE [73], COMPTEL [48], and INTEGRAL [49] at all energy bands considered. The COMPTEL and INTEGRAL constraints probe hard X-ray and soft gamma-ray emission mechanisms not included in our model and are not binding on the CR populations considered here.
4. *Tension with observed Fermi-LAT spectra.* Despite the order-of-magnitude agreement in flux normalization at R_{trunc} , the observed Fermi-LAT spectral index $\Gamma = -3.61 \pm 0.33$ is substantially softer than the hadronic prediction $\Gamma_{\text{had}} \approx -2.4$ to -2.6 , and cannot be reproduced by any physically motivated hadronic model. This tension suggests that either background source contamination contributes to the reported signal, or that the CRp spectrum in A3667 has been modified by reacceleration and transport processes beyond the scope of a simple power-law model.

The results presented here demonstrate that A3667 is a promising but challenging target for non-thermal emission studies. We note, however, that the final flux estimates presented in this work are subject to several modelling uncertainties that have not been fully quantified, including uncertainties in the CR proton distribution,

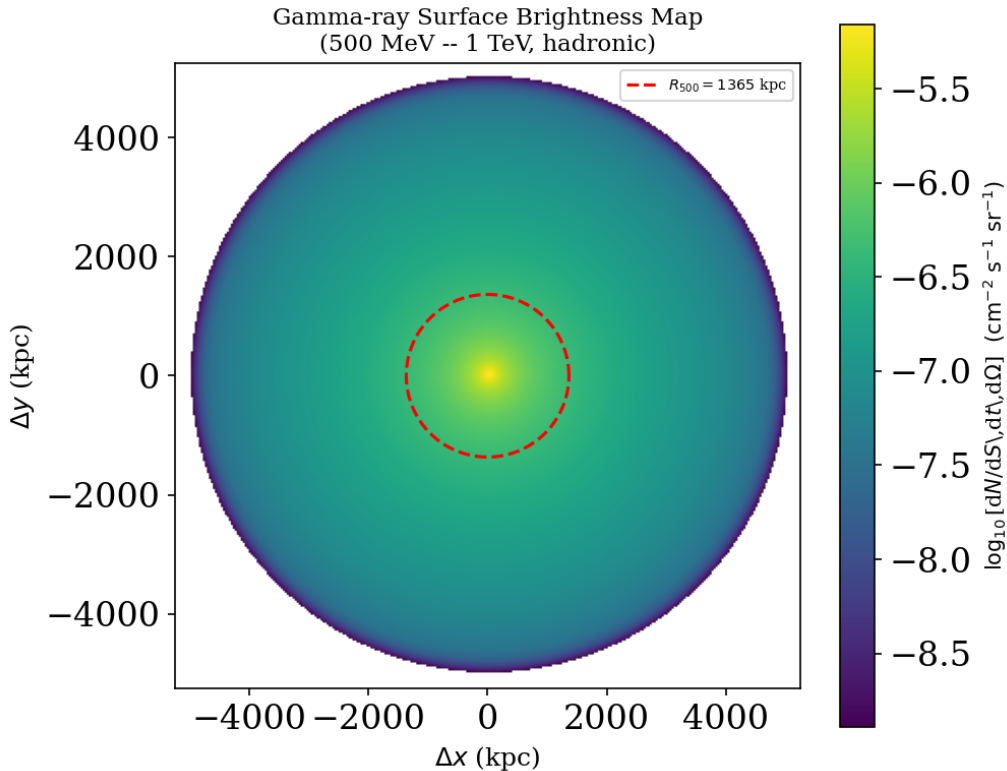


FIG. 9: Predicted gamma-ray surface brightness map of A3667 in the 500 MeV–1 TeV band from hadronic pp interactions, shown on a logarithmic colour scale. The red dashed circle marks $R_{500} = 1365$ kpc. The map is clipped to $\pm R_{\text{trunc}}$ in both axes. The circular symmetry reflects the azimuthally averaged input profiles; real asymmetries due to the merging morphology are not included.

magnetic field structure, gas density profile, and spatial integration region. Consequently, our results should be interpreted primarily at the order-of-magnitude level rather than as precise flux predictions. Several directions for future work are warranted. Future work will incorporate spatially resolved radio observations emission in A3667 to better constrain the non-thermal emission. The Cherenkov Telescope Array (CTA) will provide an order-of-magnitude improvement in point-source sensitivity in the 0.1–100 TeV range and will be optimally positioned for southern-sky targets such as A3667 [74]. All calculations in this work assume spherical symmetry and azimuthally averaged profiles. A3667’s prominent double radio relics and cold fronts indicate a strongly asymmetric ICM structure [41, 42, 46]. A full three-dimensional model incorporating the spatial distribution of the merger shocks, the anisotropic CR injection at the relic positions, and the asymmetric gas distribution will be necessary to make quantitative predictions for the surface brightness morphology that can be tested with future spatially resolved gamma-ray observations.

VI. ACKNOWLEDGEMENTS

SM gratefully acknowledges the Ministry of Education (MoE), Government of India, for their consistent support through the research fellowship, which has been instrumental in facilitating the successful completion of this work.

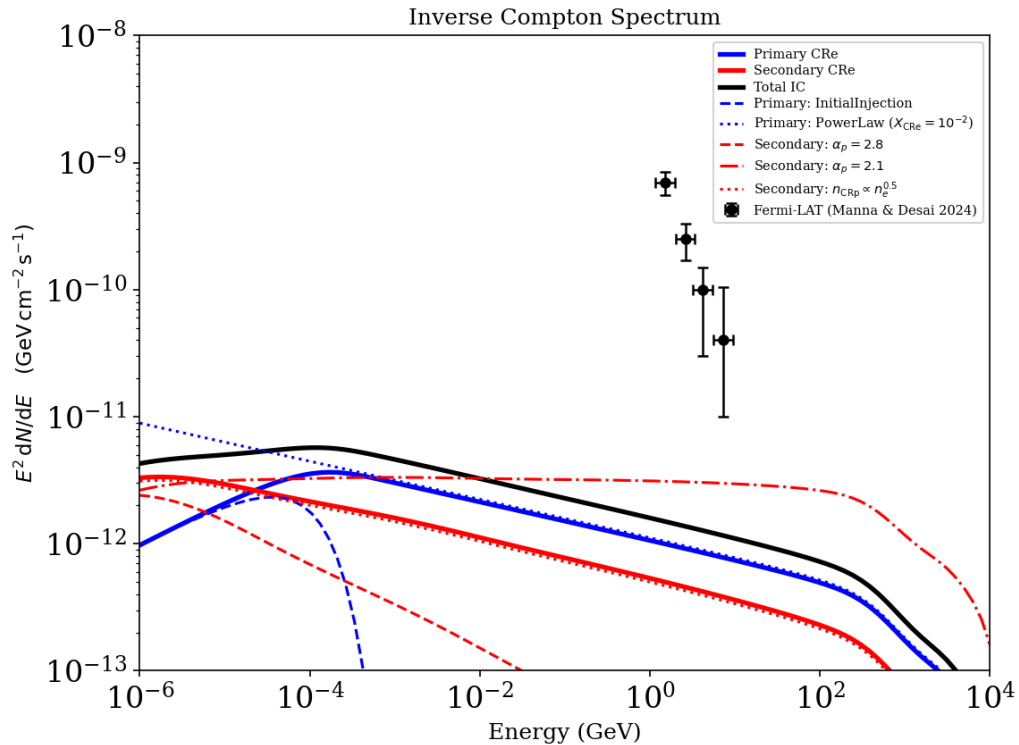


FIG. 10: Predicted IC spectral energy distribution of A3667 integrated over the full cluster volume to R_{trunc} . The solid blue and red curves show the primary and secondary CRE contributions respectively; the solid black curve shows their sum. Dashed and dotted blue curves show spectral model variations for the primary CRE: **InitialInjection** (cooled spectrum) and a steeper power-law with $X_{\text{CRE}} = 10^{-2}$. Dashed and dash-dotted red curves show secondary IC emission for $\alpha_p = 2.8$ and $\alpha_p = 2.1$ respectively; the dotted red curve shows the effect of a shallower CRp spatial profile ($\eta = 0.5$, $n_{\text{CRp}} \propto n_e^{0.5}$). Black flux points show the Fermi-LAT measurements from Manna and Desai [16] in the 1–10 GeV range. The IC emission lies well below the Fermi-LAT detections, confirming that the observed gamma-ray flux is dominated by hadronic pp emission rather than inverse Compton scattering off the CMB.

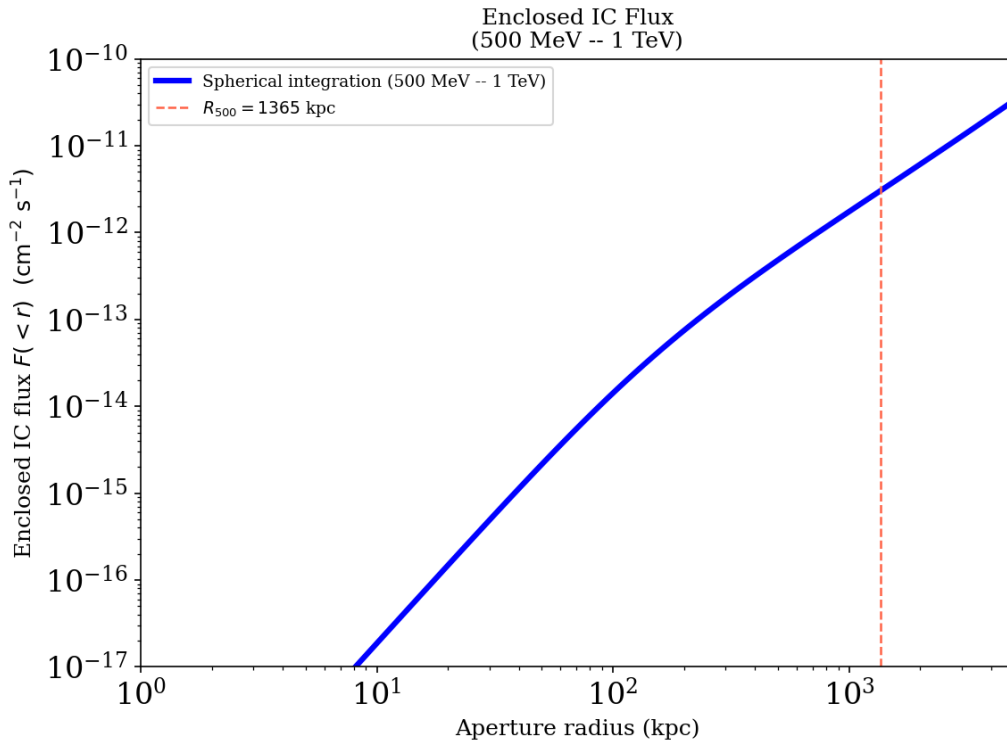


FIG. 11: Enclosed IC flux $F_{\text{IC}}(< r)$ as a function of aperture radius for A3667 in the 500 MeV–1 TeV band from spherical integration. The flux continues to rise steeply beyond R_{500} (red dashed), with $\sim 91\%$ of the total IC emission originating from $r > R_{500}$, reflecting the more extended CRe distribution compared to the hadronic case.

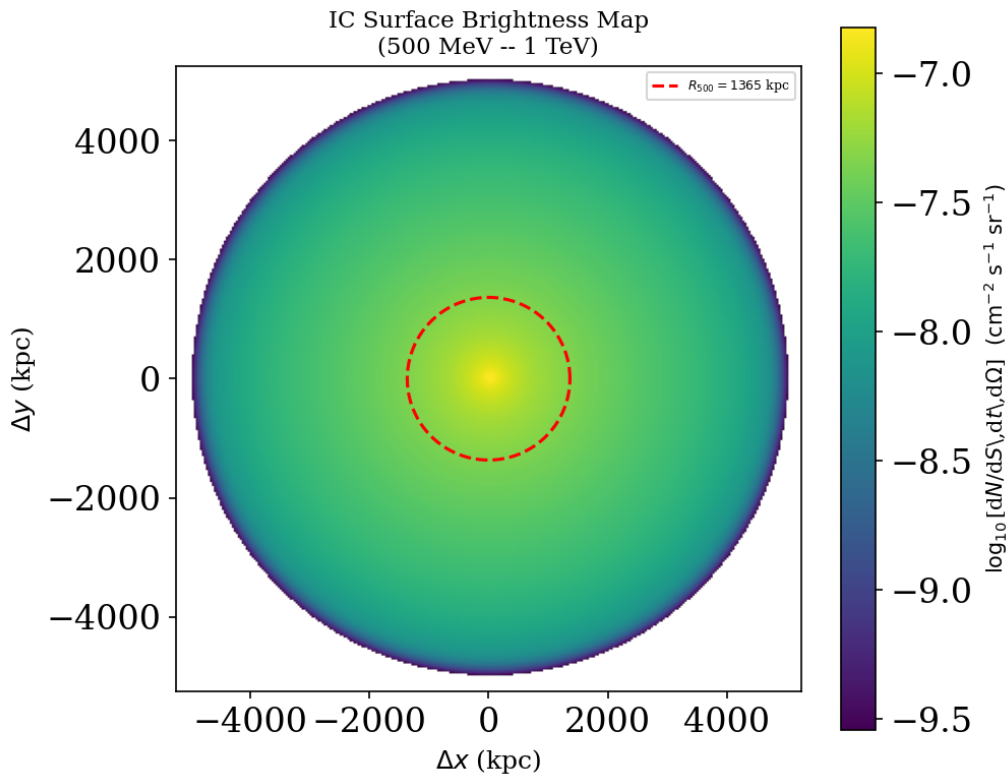


FIG. 12: Predicted IC surface brightness map of A3667 in the 500 MeV–1 TeV band, shown on a logarithmic colour scale. The red dashed circle marks $R_{500} = 1365$ kpc. The map is clipped to $\pm R_{\text{trunc}}$ in both axes. Compared to the hadronic pion-decay map, the IC emission is more spatially extended with a shallower central concentration, reflecting the linear rather than quadratic dependence of the IC emissivity on the thermal gas density.

-
- [1] S. D. M. White and M. J. Rees, *MNRAS* **183**, 341 (1978).
- [2] A. V. Kravtsov and S. Borgani, *Ann. Rev. Astron. Astrophys.* **50**, 353 (2012), 1205.5556.
- [3] S. W. Allen, A. E. Evrard, and A. B. Mantz, *Ann. Rev. Astron. Astrophys.* **49**, 409 (2011), 1103.4829.
- [4] A. A. Vikhlinin, A. V. Kravtsov, M. L. Markevich, R. A. Sunyaev, and E. M. Churazov, *Physics Uspekhi* **57**, 317-341 (2014).
- [5] H. Miyatake, arXiv e-prints arXiv:2505.07697 (2025), 2505.07697.
- [6] H. Böhringer and G. Chon, *Modern Physics Letters A* **31**, 1640008 (2016), 1610.02855.
- [7] S. Desai, *Physics Letters B* **778**, 325 (2018), 1708.06502.
- [8] K. Bora and S. Desai, *JCAP* **2021**, 012 (2021), 2008.10541.
- [9] K. Bora and S. Desai, *JCAP* **2021**, 052 (2021), 2104.00974.
- [10] K. Bora, R. F. L. Holanda, S. Desai, and S. H. Pereira, *European Physical Journal C* **82**, 17 (2022), 2106.15805.
- [11] L. Feretti, G. Giovannini, F. Govoni, and M.urgia, *Astronomy and Astrophysics Review* **20**, 54 (2012), 1205.1919.
- [12] D. R. Wik, A. Hornstrup, S. Molendi, G. Madejski, F. A. Harrison, A. Zoglauer, B. W. Grefenstette, F. Gastaldello, K. K. Madsen, N. J. Westergaard, et al., *Astrophys. J.* **792**, 48 (2014), 1403.2722.
- [13] M. Ackermann, M. Ajello, A. Allafort, L. Baldini, J. Ballet, G. Barbiellini, D. Bastieri, K. Bechtol, R. Bellazzini, R. D. Blandford, et al., *JCAP* **2010**, 025 (2010), 1002.2239.
- [14] M. Ackermann, M. Ajello, A. Albert, A. Allafort, W. B. Atwood, L. Baldini, J. Ballet, G. Barbiellini, D. Bastieri, K. Bechtol, et al., *Astrophys. J.* **787**, 18 (2014), 1308.5654.
- [15] M. Ackermann, A. Albert, W. B. Atwood, L. Baldini, J. Ballet, G. Barbiellini, D. Bastieri, R. Bellazzini, E. Bissaldi, E. D. Bloom, et al., *Astron. & Astrophys.* **586**, A71 (2016), 1509.06903.
- [16] S. Manna and S. Desai, *JCAP* **2024**, 017 (2024), 2310.07519.
- [17] G. D. Harale and S. Paul, *Phys. Rev. D* **112**, 103025 (2025), 2511.15559.
- [18] S. Li and F. Han, *Astrophys. J.* **997**, 227 (2026).
- [19] I. Reiss and U. Keshet, *JCAP* **2018**, 010 (2018), 1705.05376.
- [20] U. Keshet, *JCAP* **2025**, 016 (2025), 2502.19494.
- [21] U. Keshet, arXiv e-prints arXiv:2503.09687 (2025), 2503.09687.
- [22] S. Manna and S. Desai, *Physics of the Dark Universe* **49**, 101966 (2025), 2502.15235.
- [23] G. Brunetti and T. W. Jones, *International Journal of Modern Physics D* **23**, 1430007-98 (2014), 1401.7519.
- [24] D. Wittor, *Universe* **9**, 319 (2023).
- [25] S. Paul, R. Kale, A. Datta, A. Basu, S. Sur, V. Parekh, P. Gupta, S. Chatterjee, S. Salunkhe, A. Iqbal, et al., *Journal of Astrophysics and Astronomy* **44**, 38 (2023), 2211.01393.
- [26] T. A. Ensslin, P. L. Biermann, P. P. Kronberg, and X.-P. Wu, *Astrophys. J.* **477**, 560 (1997), astro-ph/9609190.
- [27] J. A. Hinton, W. Domainko, and E. C. D. Pope, *MNRAS* **382**, 466 (2007), astro-ph/0701033.
- [28] F. Vazza, M. Brüggén, D. Wittor, C. Gheller, D. Eckert, and M. Stubbe, *MNRAS* **459**, 70 (2016), 1603.02688.
- [29] V. Petrosian, *Astrophys. J.* **557**, 560 (2001), astro-ph/0101145.
- [30] G. Brunetti, S. Zimmer, and F. Zandanel, *MNRAS* **472**, 1506 (2017), 1707.02085.
- [31] S. Hussain, R. Alves Batista, E. M. de Gouveia Dal Pino, and K. Dolag, *Nature Communications* **14**, 2486 (2023), 2203.01260.
- [32] M. Di Mauro, J. Pérez-Romero, M. A. Sánchez-Conde, and N. Fornengo, *Phys. Rev. D* **107**, 083030 (2023), 2303.16930.
- [33] D. Song, K. Murase, and A. Kheirandish, arXiv e-prints arXiv:2308.00589 (2023), 2308.00589.
- [34] E. M. Storm, T. E. Jeltema, and S. Profumo, *Astrophys. J.* **755**, 117 (2012), 1206.1676.
- [35] P. Blasi, S. Burles, and A. V. Olinto, *Astrophys. J. Lett.* **514**, L79 (1999), astro-ph/9812487.
- [36] C. Pfrommer, T. A. Enklin, and V. Springel, *MNRAS* **385**, 1211 (2008).
- [37] F. Miniati, *MNRAS* **342**, 1009 (2003), astro-ph/0303593.
- [38] A. Pinzke and C. Pfrommer, *MNRAS* **409**, 449 (2010), 1001.5023.
- [39] Y. Rephaeli, *Astrophys. J.* **227**, 364 (1979).
- [40] A. Reimer, O. Reimer, R. Schlickeiser, and A. Iyudin, *Astron. & Astrophys.* **424**, 773 (2004), astro-ph/0405224.
- [41] M. S. Owers, W. J. Couch, and P. E. J. Nulsen, *Astrophys. J.* **693**, 901 (2009), 0811.3031.
- [42] M. Johnston-Hollitt, R. W. Hunstead, and E. Corbett, *Astron. & Astrophys.* **479**, 1 (2008), 0711.4129.
- [43] L. Hindson, M. Johnston-Hollitt, N. Hurley-Walker, K. Buckley, J. Morgan, E. Carretti, K. S. Dwarakanath, M. Bell, G. Bernardi, N. D. R. Bhat, et al., *MNRAS* **445**, 330 (2014), 1408.3167.
- [44] Y. Omiya, K. Nakazawa, T. Tamura, H. Akamatsu, K. Matsushita, N. Okabe, K. Sato, Y. Fujita, L. Gu, A. Simionescu, et al., arXiv e-prints arXiv:2403.10150 (2024), 2403.10150.
- [45] F. de Gasperin, L. Rudnick, A. Finoguenov, D. Wittor, H. Akamatsu, M. Brüggén, J. O. Chibueze, T. E. Clarke, W. Cotton, V. Cuciti, et al., *Astron. & Astrophys.* **659**, A146 (2022), 2111.06940.
- [46] A. Vikhlinin, M. Markevitch, and S. S. Murray, *Astrophys. J.* **551**, 160 (2001), astro-ph/0008496.
- [47] S. Li and F. Han, *Astrophys. J.* **997**, 227 (2026).
- [48] S. Manna and S. Desai, *JCAP* **2024**, 013 (2024), 2401.13240.
- [49] S. Manna, S. Desai, and R. A. Krivonos, arXiv e-prints arXiv:2512.12616 (2025), 2512.12616.
- [50] J. Chang, G. Ambrosi, Q. An, R. Asfandiyarov, P. Azzarello, P. Bernardini, B. Bertucci, M. S. Cai, M. Caragiulo, D. Y. Chen, et al., *Astroparticle Physics* **95**, 6 (2017), 1706.08453.
- [51] J. Chang, *Chinese Journal of Space Science* **34**, 550 (2014).
- [52] G. Ambrosi, Q. An, R. Asfandiyarov, P. Azzarello, P. Bernardini, M. S. Cai, M. Caragiulo, J. Chang, D. Y. Chen,

- H. F. Chen, et al., *Astroparticle Physics* **106**, 18 (2019), 1907.02173.
- [53] S. Manna and S. Desai, *Journal of High Energy Astrophysics* **44**, 210 (2024), 2408.10983.
- [54] M. Ajello, P. Rebusco, N. Cappelluti, O. Reimer, H. Böhringer, V. La Parola, and G. Cusumano, *Astrophys. J.* **725**, 1688 (2010), 1009.4699.
- [55] M. S. Mirakhor and S. A. Walker, *Publications of the Astronomical Society of Australia* **42**, e090 (2025), 2505.20453.
- [56] K. Nakazawa, C. L. Sarazin, M. Kawaharada, T. Kitaguchi, S. Okuyama, K. Makishima, N. Kawano, Y. Fukazawa, S. Inoue, M. Takizawa, et al., *Publications of the Astronomical Society of Japan* **61**, 339 (2009), 0812.1438.
- [57] R. Adam, H. Goksu, A. Leingärtner-Goth, S. Etti, R. Gnatyk, B. Hnatyk, M. Hütten, J. Pérez-Romero, M. A. Sánchez-Conde, and O. Sergijenko, *Astron. & Astrophys.* **644**, A70 (2020), 2009.05373.
- [58] V. V. Voitsekhovskiy, *Advances in Astronomy and Space Physics* **11**, 13 (2021), 2201.09606.
- [59] K. W. Cavagnolo, M. Donahue, G. M. Voit, and M. Sun, *Astrophys. J. Suppl. Ser.* **182**, 12 (2009), 0902.1802.
- [60] Planck Collaboration, P. A. R. Ade, N. Aghanim, M. Arnaud, M. Ashdown, J. Aumont, C. Baccigalupi, A. J. Banday, R. B. Barreiro, J. G. Bartlett, et al., *Astron. & Astrophys.* **594**, A13 (2016), 1502.01589.
- [61] L. E. Bleem, B. Stalder, T. de Haan, K. A. Aird, S. W. Allen, D. E. Applegate, M. L. N. Ashby, M. Bautz, M. Bayliss, B. A. Benson, et al., *Astrophys. J. Suppl. Ser.* **216**, 27 (2015), 1409.0850.
- [62] E. Bulbul, A. Liu, M. Kluge, X. Zhang, J. S. Sanders, Y. E. Bahar, V. Ghirardini, E. Artis, R. Seppi, C. Garrel, et al., *Astron. & Astrophys.* **685**, A106 (2024), 2402.08452.
- [63] A. Cavaliere and R. Fusco-Femiano, *Astron. & Astrophys.* **49**, 137 (1976).
- [64] M. Murgia, F. Govoni, L. Feretti, G. Giovannini, D. Dallacasa, R. Fanti, G. B. Taylor, and K. Dolag, *Astron. & Astrophys.* **424**, 429 (2004), astro-ph/0406225.
- [65] A. Bonafede, L. Feretti, M. Murgia, F. Govoni, G. Giovannini, D. Dallacasa, K. Dolag, and G. B. Taylor, *Astron. & Astrophys.* **513**, A30 (2010), 1002.0594.
- [66] D. Ryu, H. Kang, E. Hallman, and T. W. Jones, *Astrophys. J.* **593**, 599 (2003), astro-ph/0305164.
- [67] H. Kang and T. W. Jones, *Astroparticle Physics* **28**, 232 (2007), 0705.3274.
- [68] T. Sjöstrand, S. Ask, J. R. Christiansen, R. Corke, N. Desai, P. Ilten, S. Mrenna, S. Prestel, C. O. Rasmussen, and P. Z. Skands, *Computer Physics Communications* **191**, 159 (2015), 1410.3012.
- [69] E. Kafexhiu, F. Aharonian, A. M. Taylor, and G. S. Vila, *Phys. Rev. D* **90**, 123014 (2014), 1406.7369.
- [70] M. S. Longair, *High Energy Astrophysics* (2011).
- [71] A. Domínguez, J. R. Primack, D. J. Rosario, F. Prada, R. C. Gilmore, S. M. Faber, D. C. Koo, R. S. Somerville, M. A. Pérez-Torres, P. Pérez-González, et al., *MNRAS* **410**, 2556 (2011), 1007.1459.
- [72] R. Caputo, M. Ajello, C. A. Kierans, J. S. Perkins, J. L. Racusin, L. Baldini, M. G. Baring, E. Bissaldi, E. Burns, N. Cannady, et al., *Journal of Astronomical Telescopes, Instruments, and Systems* **8**, 044003 (2022), 2208.04990.
- [73] S. Manna and S. Desai, *Journal of High Energy Astrophysics* **44**, 210 (2024), 2408.10983.
- [74] W. Hofmann and R. Zanin, arXiv e-prints arXiv:2305.12888 (2023), 2305.12888.
- [75] G. M. Voit, S. T. Kay, and G. L. Bryan, *MNRAS* **364**, 909 (2005), astro-ph/0511252.
- [76] M. Arnaud, G. W. Pratt, R. Piffaretti, H. Böhringer, J. H. Croston, and E. Pointecouteau, *Astron. & Astrophys.* **517**, A92 (2010), 0910.1234.

Appendix A: Derived Thermodynamic Profiles of A3667

This appendix presents the full set of derived thermodynamic and structural profiles of A3667 obtained from the density and pressure models described in Section II C. The electron density (β -model), thermal pressure ($P = n_e \times T$), and temperature (power-law) profiles are shown individually in the main text (Figures 4–6); the six derived quantities discussed below are collected in Figure 13. All profiles are evaluated on a logarithmic radial grid spanning 10–5000 kpc.

1. Entropy Profile

The ICM entropy is shown in panel (a) of Figure 13. The profile increases monotonically and confirms that the pressure model satisfies the thermodynamic requirement $dK/dr > 0$ [75] across all radii.

2. Enclosed Thermal Energy

The enclosed thermal energy $U_{\text{th}}(< r)$ is shown in panel (b) of Figure 13. The profile reaches $U_{\text{th}}(< R_{500}) \sim 10^{63}$ erg, typical for a cluster of this mass at low redshift [76].

3. Gas Mass Profile

The enclosed gas mass $M_{\text{gas}}(< r)$ is shown in panel (c). The gas fraction $f_{\text{gas}} = M_{\text{gas}}/M_{500}$ approaches ~ 0.15 – 0.18 near R_{500} , broadly consistent with the cosmic baryon fraction $f_b = \Omega_b/\Omega_m = 0.158$ [60], as shown in panel (e).

4. Hydrostatic Mass Profile and HSE Bias

The hydrostatic equilibrium (HSE) mass profile $M_{\text{HSE}}(< r)$, shown in panel (d), is derived analytically from the X-ray temperature and density profiles under the assumption of spherical symmetry and thermal pressure support. The ACCEPT thermodynamic data extend only to $0.216 R_{500} = 295$ kpc. The evaluation of $M_{\text{HSE}}(R_{500})$ therefore relies entirely on the extrapolated β -model density and power-law temperature profiles beyond the data boundary. The result is model-dependent and should not be interpreted as a direct observational constraint.

5. Gas Fraction Profile

The cumulative gas fraction $f_{\text{gas}}(< r) = M_{\text{gas}}(< r)/M_{\text{HSE}}(< r)$ is shown in panel (e), with the cosmic baryon fraction $f_b = \Omega_b/\Omega_m = 0.158$ [60] overlaid as a reference. The gas fraction rises steeply at small radii and approaches the cosmic baryon fraction near R_{500} .

6. Overdensity Profile

The mean overdensity contrast $\Delta(r) \equiv \bar{\rho}(< r)/\rho_c(z)$, where $\bar{\rho}(< r) = 3M_{\text{HSE}}(< r)/(4\pi r^3)$ is the mean enclosed mass density, is shown in panel (f). The radius at which $\Delta = 500$ defines R_{500}^{HSE} from the profile, indicated by the dashed vertical line. This value is consistent with the input $R_{500} = 1365.5$ kpc derived from the SPT-SZ mass (Section II A), confirming internal consistency of the thermodynamic modelling.

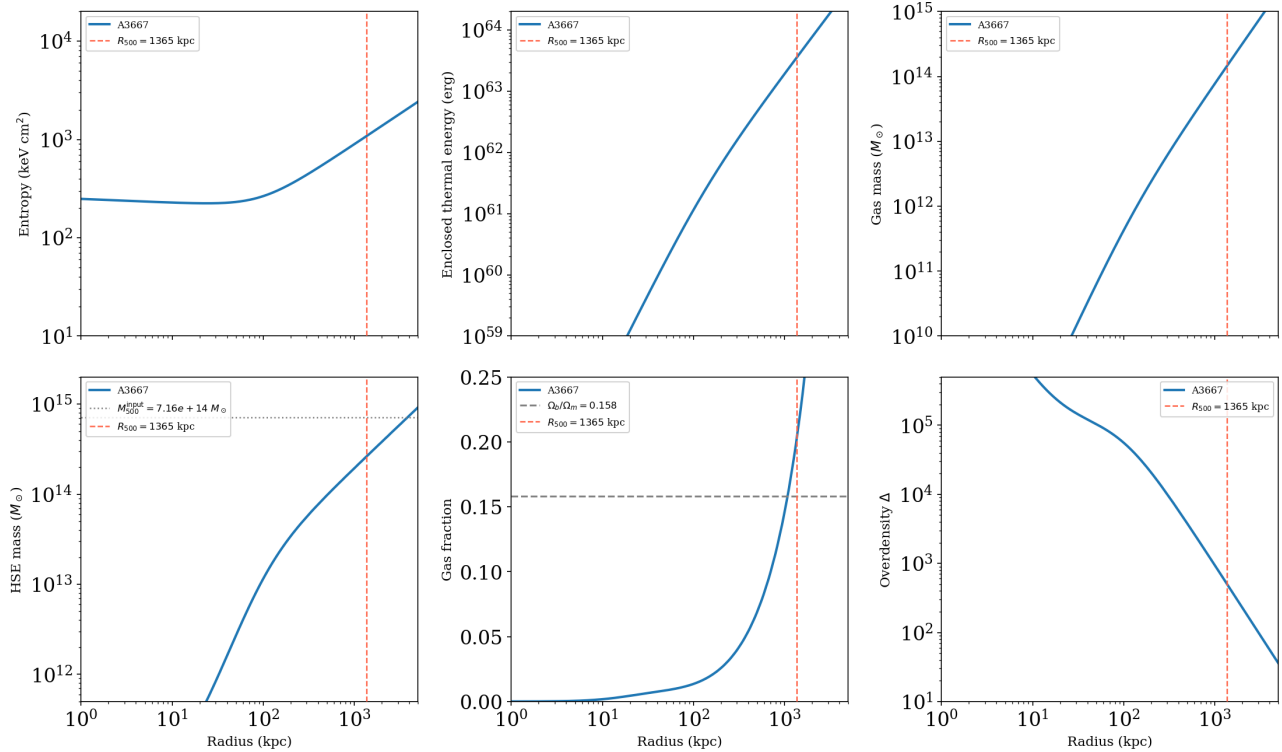


FIG. 13: Derived thermodynamic profiles of A3667 evaluated from the β -model density and power-law temperature profiles over 10–5000 kpc. (a) ICM entropy. (b) Enclosed thermal energy $U_{\text{th}}(< r)$. (c) Enclosed gas mass $M_{\text{gas}}(< r)$. (d) Hydrostatic mass $M_{\text{HSE}}(< r)$. (e) Cumulative gas fraction $f_{\text{gas}}(< r) = M_{\text{gas}}/M_{\text{HSE}}$; the horizontal dashed line marks the cosmic baryon fraction $f_b = 0.158$ [60]. (f) Overdensity contrast $\Delta(r)$; the vertical dashed line marks R_{500}^{HSE} and the horizontal dotted line marks $\Delta = 500$. In all panels the vertical red dashed line marks $R_{500} = 1365.5$ kpc from the SPT-SZ mass. All profiles are model-dependent beyond $r \approx 295$ kpc ($0.22 R_{500}$), the outermost radius of the ACCEPT data.